



# Mo-doped Ni<sub>3</sub>S<sub>4</sub> nanosheets grown on carbonized wood as highly efficient and durable electrocatalysts for water splitting

Zhikai Shi<sup>a</sup>, Chengwei Mao<sup>a</sup>, Lei Zhong<sup>a</sup>, Jiayao Peng<sup>a</sup>, Meilin Liu<sup>c</sup>, Hexing Li<sup>b</sup>, Jianlin Huang<sup>a,\*</sup>

<sup>a</sup> School of Environment and Energy, Guangdong Provincial Key Laboratory of Solid Wastes Pollution Control and Recycling, South China University of Technology, Guangzhou 510006, China

<sup>b</sup> The Education Ministry Key Lab of Resource Chemistry and Shanghai Key Laboratory of Rare Earth Functional Materials, Shanghai Normal University, Shanghai 200234, China

<sup>c</sup> School of Materials Science and Engineering, Georgia Institute of Technology, Atlanta, GA 30332-0245, USA

## ARTICLE INFO

### Keywords:

Lattice expansion  
Mo-doped Ni<sub>3</sub>S<sub>4</sub>  
Carbonized wood  
Overall water splitting  
DFT calculations

## ABSTRACT

Rational design and fabrication of nonprecious metal-based electrocatalysts with high activity and excellent stability for overall water splitting (OWS) is still a grand challenge. Here we report a novel electrocatalyst constructed by incorporating molybdenum into the Ni<sub>3</sub>S<sub>4</sub> lattices grown on carbonized wood (denoted as Mo-Ni<sub>3</sub>S<sub>4</sub>/CW). Experimental results and density functional theory (DFT)-based calculations demonstrate that lattice expansion of Ni<sub>3</sub>S<sub>4</sub> caused by Mo doping optimizes adsorption energy of hydrogen/oxygen species and regulates local charge density of active sites, which promote the oxygen evolution reaction (OER) and hydrogen evolution reaction (HER). Also, a nickel (oxy)hydroxide (Ni-OOH) layer generated via surface reconstruction of Ni<sub>3</sub>S<sub>4</sub> nanosheets improves the intrinsic activity for OER. Moreover, the 3D low-tortuosity porous CW substrate increases the exposure of active specific surface, accelerates the rates of electron transfer, electrolyte diffusion, and gas products escaping. Accordingly, an optimized electrocatalyst (Mo-Ni<sub>3</sub>S<sub>4</sub>/CW-0.4) exhibits ultralow overpotentials of 17 and 240 mV for HER and OER at 10 mA cm<sup>-2</sup>, respectively. Besides, an electrolyzer composed of Mo-Ni<sub>3</sub>S<sub>4</sub>/CW-0.4 electrodes as both the anode and cathode shows a low cell voltage of 1.46 V at 10 mA cm<sup>-2</sup> while maintaining superior durability over 50 h for OWS. Further, it requires only 0.19 V to achieve 10 mA cm<sup>-2</sup> for hydrazine oxidation-assisted water electrolysis, indicating highly attractive potential for economical hydrogen production coupling with pollutants treatment.

## 1. Introduction

Electrocatalytic water splitting for Hydrogen (H<sub>2</sub>) generation is considered a highly attractive and promising technology because it can be driven by renewable electricity (e.g., solar, wind energy etc.) [1–3]. The water splitting consists of the oxygen evolution reaction (OER) on the anode and hydrogen evolution reaction (HER) on the cathode of cell. It has been widely accepted that the electrocatalysts based on noble metals (e.g., Pt and Ru/IrO<sub>2</sub>) usually exhibit a superior performance for HER and OER [4,5]. However, their scarcity, expensiveness, and unsatisfied durability seriously impede their large-scale industrial applications. Accordingly, rational design and construction of a bifunctional catalyst with low-cost, high-efficiency, and long-term stability for water electrolysis is still highly desirable but challenging.

Transition metal sulfides (TMSs) have attracted much attention due to their low-cost, good electrical conductivity, and high intrinsic catalytic activity [6,7]. However, pure TMSs usually present an unfavorable electrocatalytic performance, due possibly to insufficient exposure of active sites, easily aggregation, and poor durability under the conditions for water electrolysis. Lattice engineering through doing is an efficient strategy to enhance electrocatalytic performance of transition metal-based catalysts owing to the redistribution of local charge density and improvement of intrinsic activity [8]. For example, Qin et al. reported the electrochemical lithium intercalation method to improve the activity and stability of RuO<sub>2</sub> for acidic OER [9]. Wang et al. prepared V-doped CoP<sub>2</sub> porous nanowires loaded on carbon cloth as high-efficiency electrocatalysts for acid water decomposition [10]. Sun et al. presented that NiFeRh-LDH nanosheets were prepared on Ni foam

\* Corresponding author.

E-mail address: [jianlinhuang@scut.edu.cn](mailto:jianlinhuang@scut.edu.cn) (J. Huang).

<https://doi.org/10.1016/j.apcatb.2023.123123>

Received 13 May 2023; Received in revised form 10 July 2023; Accepted 18 July 2023

Available online 20 July 2023

0926-3373/© 2023 Elsevier B.V. All rights reserved.

by doping Rh into NiFe-LDH matrix, which exhibited outstanding overall water splitting [11]. In addition, it is of great importance to construct electrocatalysts with highly exposed active sites and superior electrical conductivity toward improving the catalytic performance of OWS [12]. Thus, some conductive substrates (e.g., metal foam [13], carbon cloth [14], graphene [15], and carbon nanotube [16]) have been widely used as supports to load active materials for constructing highly efficient electrocatalysts. Nevertheless, these synthetic methods usually involve expensive and harmful chemicals and/or complicated preparation processes, which are incompatible with green and sustainable development. Additionally, simply physical deposition and combination often result in undesirable disordered micro-morphology/structure, low exposure of active sites, and structural instability of catalysts. Accordingly, it is highly desirable and urgent to explore eco-friendly, renewable, and low-cost electrocatalysts with high performance and excellent durability for OWS.

Wood is an abundant, green, and renewable resource. In recent years, wood derived nanomaterials have obtained increasing interest thanks to their high value-added utilization [17–20]. The preparation of high-performance electrocatalysts using carbonized wood (CW) as a support has also been widely studied due to its 3D hierarchically porous structure, low-tortuosity microchannels, tunable hydrophilicity/hydrophobicity, and good mechanical properties [21–23]. These features endow a perfect skeleton of the CW to construct highly efficient tri-phase reaction interface of gas, liquid, and solid for OWS. Although several important progresses have been made, the detailed structure-performance relationship and reaction mechanism are yet to be fully understood for wood-based electrocatalysts for OWS.

Herein, we reported a novel bifunctional electrocatalyst consisted of molybdenum-doped nickel sulfide nanosheets tightly grown in situ on carbonized wood (Mo-Ni<sub>3</sub>S<sub>4</sub>/CW). The obtained Mo-Ni<sub>3</sub>S<sub>4</sub>/CW catalyst for OWS not only retains the 3D low-tortuosity porous structure of natural wood but also regulates local electronic structure and optimizes adsorption energy of hydrogen and oxygen intermediates through Mo-incorporated Ni<sub>3</sub>S<sub>4</sub> nanosheets with lattice expansion. As a result, the optimal Mo-Ni<sub>3</sub>S<sub>4</sub>/CW-0.4 catalyst displays HER and OER activity with ultralow overpotentials of 17 and 240 mV to attain current density of 10 mA cm<sup>-2</sup> in alkaline electrolyte, respectively. An electrolyzer composed of two identical Mo-Ni<sub>3</sub>S<sub>4</sub>/CW-0.4 electrodes shows superior OWS activity with a low cell voltage of 1.46 V at 10 mA cm<sup>-2</sup>, as well as preserves its initial performance without obvious voltage decay after continuous operation of 50 h. Impressively, it requires only 0.19 V to achieve 10 mA cm<sup>-2</sup> for hydrazine oxidation-assisted water electrolysis, suggesting its great potential for low-cost H<sub>2</sub> production. The coupling wooden carbon structure with lattice engineering provides a new strategy for the synthesis of low-cost, high-performance, and sustainable electrocatalysts for efficient water electrolysis.

## 2. Experimental

### 2.1. Chemicals and reagents

The chemicals used in this study are ACS Reagent grade, including sodium molybdate dihydrate (Na<sub>2</sub>MoO<sub>4</sub>·2 H<sub>2</sub>O, >98%), nickel nitrate hexahydrate (Ni(NO<sub>3</sub>)<sub>2</sub>·6 H<sub>2</sub>O, > 98%), thioacetamide (CH<sub>3</sub>CSNH<sub>2</sub>, >98%), absolute ethanol (C<sub>2</sub>H<sub>6</sub>O, >99%), and potassium hydroxide (KOH, >95%). These reagents are purchased from Macklin Biochemical Co. Ltd (Shanghai, China). All chemicals do not need further purification and can be used directly. Deionized water was used after purification using a pure water purifier. The natural wood (poplar) was purchased from Wood-based material factory of Guangxi in China.

### 2.2. Preparation of carbonized wood (CW)

To obtain the carbonized wood (CW) material, natural wood slices were first cut into pieces with dimensions of 2 cm × 3 cm × 1 mm,

perpendicular to the direction of growth. These wood pieces were cleaned with the water/ethanol mixed solution and dried in a vacuum oven at 80 °C for overnight. Subsequently, the dried wood pieces were carbonized in a quartz tube furnace at 500 °C for 1.5 h, and then heated to 900 °C for an additional 1.0 h in a nitrogen (N<sub>2</sub>) environment. This process resulted in the formation of a highly porous and conductive carbonized wood material.

### 2.3. Preparation of Mo-Ni<sub>3</sub>S<sub>4</sub>/CW

First, 1.0 mmol Ni(NO<sub>3</sub>)<sub>2</sub>·6 H<sub>2</sub>O, 0.4 mmol Na<sub>2</sub>MoO<sub>4</sub>·2 H<sub>2</sub>O, and 4.0 mmol thioacetamide were added into 30 mL deionized water and stirred to attain a homogeneous solution. Then, a piece of CW was added into the above solution and transferred into a 50 mL Teflon-lined stainless-steel autoclave, which was sealed and heated at 180 °C for 18 h. After cooling to room temperature, the sample was taken out and washed with deionized water for several times, and dried at 60 °C for 12 h to obtain the final samples (Mo-Ni<sub>3</sub>S<sub>4</sub>/CW). For comparison, other catalysts with different Mo-doping content were also synthesized by controlling the amount of sodium molybdate (Na<sub>2</sub>MoO<sub>4</sub>·2 H<sub>2</sub>O) used in the precursor solution. The molar ratios of Mo/Ni were 0, 0.2, 0.4, and 0.6, corresponding to Ni<sub>3</sub>S<sub>4</sub>/CW, Mo-Ni<sub>3</sub>S<sub>4</sub>/CW-0.2, Mo-Ni<sub>3</sub>S<sub>4</sub>/CW-0.4, and Mo-Ni<sub>3</sub>S<sub>4</sub>/CW-0.6 respectively. The Mo-Ni<sub>3</sub>S<sub>4</sub> samples were also prepared with similar to experimental conditions of Mo-Ni<sub>3</sub>S<sub>4</sub>/CW, excepting for without addition of CW in the precursor solution. In addition, the growth of Mo-Ni<sub>3</sub>S<sub>4</sub> on carbon paper was also prepared (denoted as Mo-Ni<sub>3</sub>S<sub>4</sub>/CP) by the same synthetic process as Mo-Ni<sub>3</sub>S<sub>4</sub>/CW and further compared their catalytic performance. The size of carbon paper is consistent with the carbonized wood. The mass loadings stay similarly. Notably, all the Mo-Ni<sub>3</sub>S<sub>4</sub>/CW catalysts can be used directly as self-standing electrodes without addition of current collectors or conductive additive/adhesives.

### 2.4. Preparation of Mo-Ni<sub>3</sub>S<sub>4</sub>/CP, Pt/C/CP and RuO<sub>2</sub>/CP

Generally, 5.0 mg as-controlled sample (Mo-Ni<sub>3</sub>S<sub>4</sub>) was mixed with 1.08 mL ethanol, 0.8 mL DI water, and 120 μL 5% Nafion dispersion within a 2 mL vial and sonicated for 30 min to obtain a homogeneous catalyst ink suspension. Subsequently, 50 μL of the catalyst ink was added dropwise onto the carbon paper (CP, 1 cm × 1 cm, 1.0 mg cm<sup>-2</sup> mass loading) to obtain the Mo-Ni<sub>3</sub>S<sub>4</sub>/CP as working electrodes. Finally, the catalyst-covered electrode was dried in a vacuum oven prior to use. The Pt/C/CP and RuO<sub>2</sub>/CP electrodes were also fabricated by the same process as Mo-Ni<sub>3</sub>S<sub>4</sub>/CP, except that the Mo-Ni<sub>3</sub>S<sub>4</sub> was replaced with the commercial 20% Pt/C or RuO<sub>2</sub>, respectively.

### 2.5. Characterizations

X-ray diffraction (XRD) was used to investigate the crystallographic information of all samples with a diffractometer (Bruker D8, USA) using a Cu Kα radiation (λ = 1.54178 Å). Raman spectra were carried out on a LabRAM HR Evolution Raman spectrometer with 532 nm laser. Field-emission scanning electron microscopy (FESEM, Hitachi SU 8010, Japan) was used to study micromorphology of samples. Transmission electron microscopy (TEM, FEI Tecnai G2 F20 S-Twin) was used to characterize the microstructure of catalysts. Elemental mapping images were collected using a TEM equipped with energy dispersive X-ray spectroscopy (EDS). X-ray photoelectron spectroscopy (XPS) measurements were conducted on a Thermo Scientific K-Alpha (USA) equipment equipped with a monochromatic Al Kα X-ray source. Nitrogen adsorption-desorption isotherms were measured by using the Brunauer-Emmett-Teller (BET; ASAP2020, America) and Barrett-Joyner-Halenda (BJH) methods. The ICP-OES analysis was performed on an inductively coupled plasma-optical emission spectrophotometer (Agilent 5110).

## 2.6. Electrochemical measurements

All electrochemical measurements were carried out in a three-electrode configuration cell using an electrochemical workstation (CHI 660E, China). The as-prepared catalyst, graphite rod, and Hg/HgO were used as the working electrode, counter electrode, and reference electrode respectively. The 1.0 M KOH electrolyte was firstly purged with  $N_2$  for 30 min to eliminate  $O_2$  before the electrochemical testing. According to the Nernst equation, all potential values were calculated relative to the reversible hydrogen electrode (RHE),  $E_{RHE} = E_{Hg/HgO} + 0.059 \times pH + 0.098 = E_{Hg/HgO} + 0.924$  V. For the OER, the overpotential ( $\eta$ ) was determined using the equation:  $\eta = E_{RHE} - 1.23$  V. Polarization curves for the HER and OER were measured using linear sweep voltammetry (LSV) at a scan rate of  $5 \text{ mV s}^{-1}$  with 95% iR correction. Electrochemical impedance spectroscopy (EIS) was measured under a scan rate of  $10 \text{ mV s}^{-1}$  with a frequency range of 0.01 Hz to 100 kHz. The electrochemically active surface areas (ECSA) of catalysts were evaluated by the double-layer capacitance ( $C_{dl}$ ) measurements using cyclic voltammetry (CV) at different scan rates of 10, 20, 30, 40, and  $50 \text{ mV s}^{-1}$  in the potential range of 0.924–1.024 V vs. RHE.

## 2.7. Density functional theory (DFT) calculations

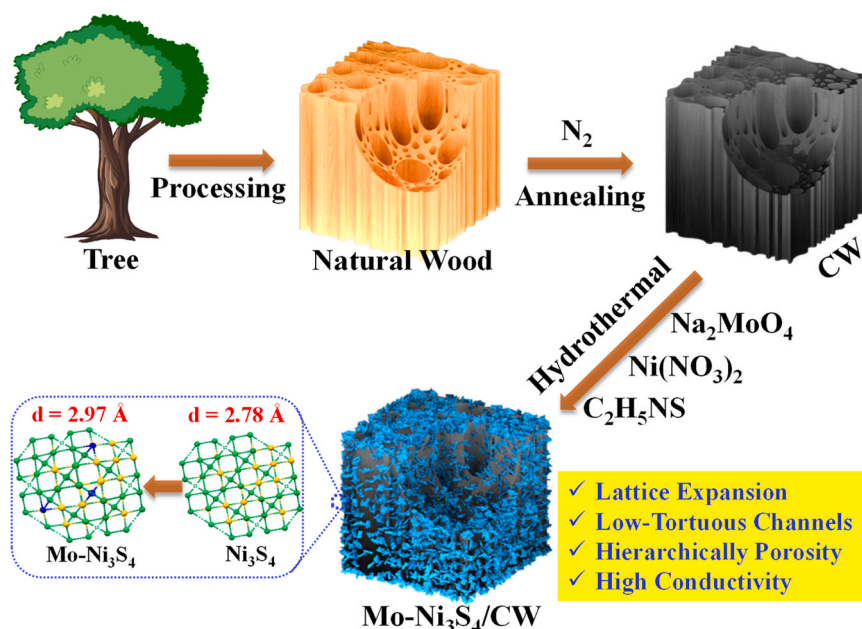
The density of states for  $Ni_3S_4$  and  $Mo-Ni_3S_4$  was investigated according to the electronic structure model acquired by the periodic DFT calculations on the CASTEP code. The reaction free energy of  $Ni_3S_4$ ,  $Mo-Ni_3S_4$ , and  $Ni-OOH$  were also studied by the periodic DFT calculations on the CASTEP code. For the (113) plane of  $Mo$ -doped  $Ni_3S_4$ , the model was fabricated by the substitution of  $Ni$  atom with  $Mo$  atom of  $Ni_3S_4$  (113) surface. A vacuum layer thickness of  $15 \text{ \AA}$  was added to eliminate the interactions between the established slabs. Meanwhile, atoms located at the bottom two layer were fixed and other atoms could be relaxed. The valence state of  $Mo$  is an average valence state obtained from the XPS results of  $Mo-Ni_3S_4$ . Generalized gradient approximation (GGA) was employed to study the electronic structure based on the Perdew, Burke and Emzerhof (PBE). For the simulation, the Quality, the Energy cut off and the k-point were set as fine, 421.80 eV and  $(3 \times 3 \times 3 \text{ \AA}^{-1})$ , respectively. The Gibbs free energy ( $G$ ) of adsorbed intermediates are calculated by:  $G = E + ZPE - TS$ , where  $E$  is the total energy obtained from DFT calculations,  $ZPE$  and  $S$  are the zero-point energy and entropy

of intermediates respectively,  $T = 298.15 \text{ K}$ . The change of free energy ( $\Delta G$ ) is calculated as:  $\Delta G = \Delta E + \Delta ZPE - T\Delta S$ , where  $\Delta E$  is the binding energy of adsorbed species. The free energies of HER and OER in alkaline media have been calculated by the Volmer-Tafel step and Four-electron transfer reaction, respectively.

## 3. Results and discussion

### 3.1. Compositional and structural characterization of catalysts

The fabrication procedure for the  $Mo$ -doped  $Ni_3S_4$  nanosheets loaded on carbonized wood ( $Mo-Ni_3S_4/CW$ ) prepared by a hydrothermal method is briefly shown in Scheme 1. First, one piece of natural wood was annealed in a tube furnace in an inert atmosphere to prepare a carbonized wood with high conductivity and highly open low-tortuosity microchannels. Subsequently,  $Mo$ -incorporated  $Ni_3S_4$  nanosheets were in-situ grown on the surface of  $CW$  channels through a hydrothermal process at  $180^\circ\text{C}$  for 18 h. Finally, the  $Mo-Ni_3S_4/CW$  sample was obtained by washing several times with deionized water and dried overnight at  $60^\circ\text{C}$  under a vacuum condition. As displayed in Fig. 1a and Fig. S2a, SEM images reveal that the  $Mo-Ni_3S_4/CW-0.4$  sample well-preserve morphological and structural features of natural wood with a 3D openly hierarchical porous structure made of some large channels with a pore size of  $\sim 100 \mu\text{m}$  and numerous small channels of  $\sim 5 \mu\text{m}$ . These porous structures possess low-tortuosity and vertical arrangement (Fig. S1), which promote electrolyte infiltration and diffusion, as well as gaseous products escaping. The existence of pits in the microchannel walls can facilitate the electrolyte rapid and homogeneous transmission thanks to interconnected 3D network structure. Compared to pure  $CW$ , the  $Mo-Ni_3S_4/CW-0.4$  has a rougher surface due to the uniform and close dispersion of abundant nanosheets on the surface of  $CW$  channel walls (Fig. 1b and Fig. S2b). The thickness of porous  $Mo$ -doped  $Ni_3S_4$  nanosheets is approximately 5 nm (Fig. 1c and Fig. S2c). Notably, the  $Mo$ -doping content in  $Mo-Ni_3S_4/CW$  samples can be simply adjusted by the amount of sodium molybdate used in the precursor solution. According to ICP-OES (Table S1), the  $Mo$  content in  $Mo-Ni_3S_4/CW-0.4$  is determined to be 0.4 wt% (Molar ratio of  $Mo/Ni = 0.33$ ), slightly smaller than that of initial amount in the precursor solution ( $Mo/Ni = 0.4$ ). It might be attributed to the incomplete  $Mo$ -doping, resulting in lower molar ratio of  $Mo/Ni$ . The content of  $Mo$ -dopant has a remarkable



**Scheme 1.** Schematic illustration of the synthesis of  $Mo-Ni_3S_4/CW$ .



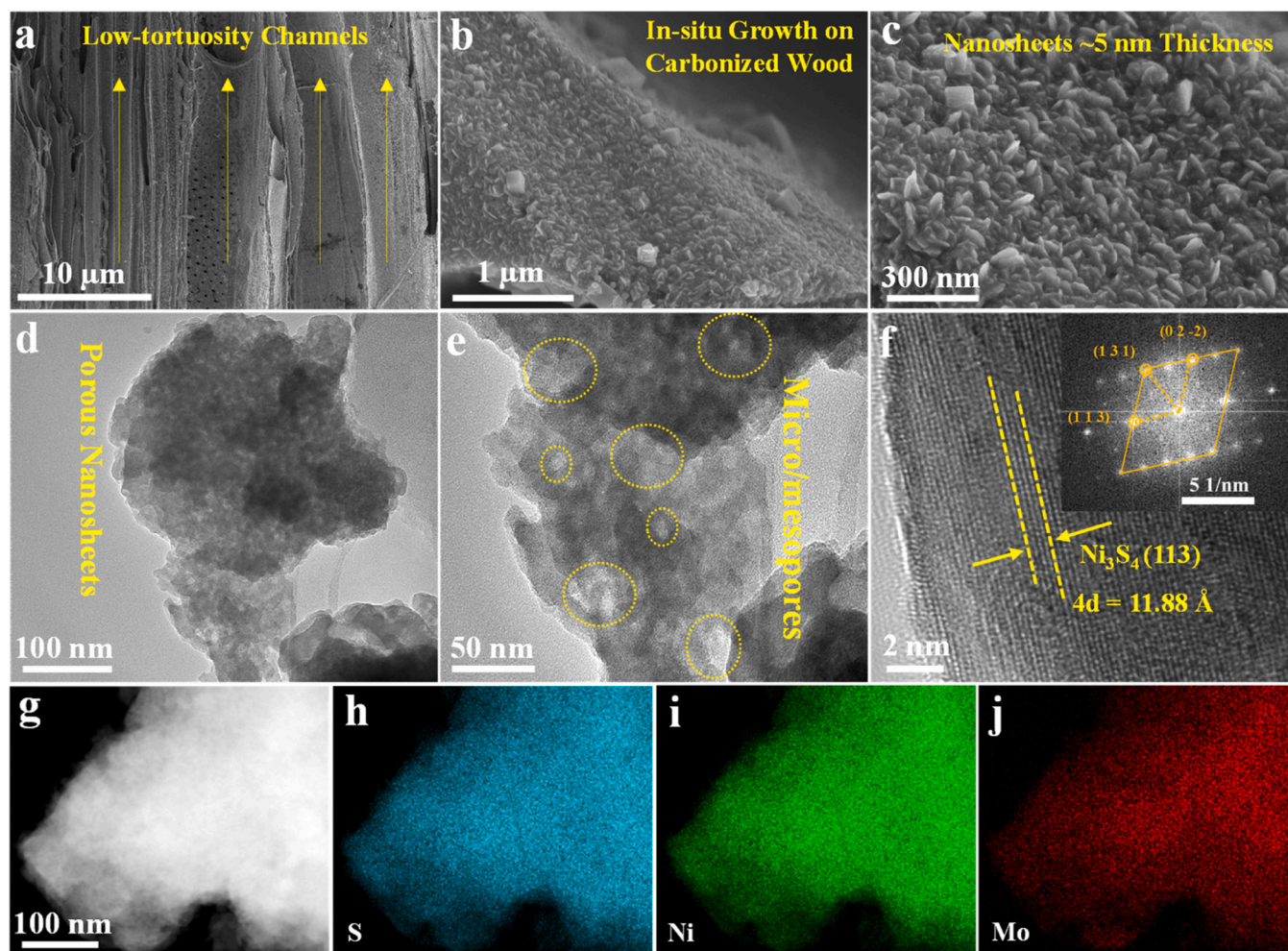


**Fig. 1.** (a–c) SEM and (d–f) TEM images of the Mo-Ni<sub>3</sub>S<sub>4</sub>/CW-0.4 at different magnifications. Inset in (f) is the SAED pattern. (g) STEM image and the corresponding elemental mappings of (h)S, (i)Ni, and (j)Mo of the Mo-Ni<sub>3</sub>S<sub>4</sub>/CW-0.4.

effect on the morphology and structure of as-obtained Mo-Ni<sub>3</sub>S<sub>4</sub>/CW samples. As shown in Fig. 1c–e, the as-prepared Mo-Ni<sub>3</sub>S<sub>4</sub>/CW-0.4 exhibits a crosslinked porous thin nanosheet structure, which is distinctively different from the bulk particles (Ni<sub>3</sub>S<sub>4</sub>/CW, Fig. S3), small nanoparticles (Mo-Ni<sub>3</sub>S<sub>4</sub>/CW-0.2, Fig. S4), and large sheets (Mo-Ni<sub>3</sub>S<sub>4</sub>/CW-0.6, Fig. S5). The differences in morphology/structure greatly affect the electrocatalytic performances (Fig. S14–S16), due likely to the differences in the interplanar spacing and porous tortuosity. Additionally, an excessive amount of Mo-doping (e.g., Mo-Ni<sub>3</sub>S<sub>4</sub>/CW-0.6) is unfavorable to electrochemical performances, due likely to the insufficient exposure of active sites. High-resolution TEM (HR-TEM) images of Ni<sub>3</sub>S<sub>4</sub>/CW clearly exhibit lattice fringes with interplanar distances of 0.278 nm, which can be indexed to the (113) planes of Ni<sub>3</sub>S<sub>4</sub> (Fig. S6a) [24]. As shown in Fig. 1f and Fig. S6c, the Mo-Ni<sub>3</sub>S<sub>4</sub>/CW-0.4 delivers an increased interplanar distance of 0.297 nm for (113) facet, proving that Mo incorporation causes lattice expansion. Moreover, the lattice distances of Ni<sub>3</sub>S<sub>4</sub> increase from 0.278 to 0.305 nm as increasing the concentration of Mo-doping (Fig. S6). The SAED pattern (inset in Fig. 1f and Fig. S2f) further demonstrates that the Ni<sub>3</sub>S<sub>4</sub> crystal structure does not change after Mo-doping [25]. STEM image and corresponding EDS mappings indicate the homogeneous distribution of Mo, Ni and S elements in Mo-Ni<sub>3</sub>S<sub>4</sub>/CW-0.4 (Fig. 1g–j and Fig. S2g–j), suggesting the successful incorporation of Mo into Ni<sub>3</sub>S<sub>4</sub>.

Compared with Ni<sub>3</sub>S<sub>4</sub>/CW, the X-ray diffraction (XRD) patterns of Mo-Ni<sub>3</sub>S<sub>4</sub>/CW samples present the relatively weak characteristic signals of Ni<sub>3</sub>S<sub>4</sub> (PDF # 43–1469) [26], suggesting the introduction of Mo atoms

decreases the crystallinity of Ni<sub>3</sub>S<sub>4</sub> (Fig. 2a). A broad peak located at 23.2° appears in all samples, which is attributed to the graphitic carbon, indicating a relatively weak degree of graphitization for the Mo-Ni<sub>3</sub>S<sub>4</sub>/CW [27]. In addition, the diffraction peak of (113) plane shifts to the lower angle from 31.68° (Ni<sub>3</sub>S<sub>4</sub>/CW) to 31.27° (Mo-Ni<sub>3</sub>S<sub>4</sub>/CW-0.6), illustrating that Mo incorporation results in a certain lattice expansion of Ni<sub>3</sub>S<sub>4</sub>. Interestingly, compared to Ni<sub>3</sub>S<sub>4</sub>, the Mo-Ni<sub>3</sub>S<sub>4</sub> samples show the diffraction peak of (113) plane shifts to higher angles as amount increase of Mo-doping (Fig. S9), indicating the lattice shrinkage of Ni<sub>3</sub>S<sub>4</sub> is occurred for Mo-Ni<sub>3</sub>S<sub>4</sub> without addition of CW in precursor solution. This phenomenon may be attributed to the Mo<sup>6+</sup> ions reduced to Mo<sup>5+</sup>/or Mo<sup>4+</sup> by the CW under hydrothermal condition [28]. The ionic radius of Mo<sup>5+</sup> and Mo<sup>4+</sup> are 0.63 and 0.65 Å respectively, slightly bigger than that of Ni<sup>3+</sup> (0.60 Å). The Mo<sup>5+</sup>/or Mo<sup>4+</sup> ions can replace partial Ni atoms and intercalate the lattice of Ni<sub>3</sub>S<sub>4</sub>, leading to lattice expansion. In contrast, for Mo-Ni<sub>3</sub>S<sub>4</sub> without CW, partial Ni ions are substituted by smaller ionic radius of Mo<sup>6+</sup> ions (0.42 Å), resulting in lattice shrinkage of Ni<sub>3</sub>S<sub>4</sub>. Compared with Ni<sub>3</sub>S<sub>4</sub>/CW, the Raman spectra (Fig. 2b) of Mo-Ni<sub>3</sub>S<sub>4</sub>/CW exhibits a new peak at ~471.4 cm<sup>-1</sup> corresponding to the vibration of Mo–S bond [29]. Additionally, there is a slightly blue-shift phenomenon of the characteristic peaks for Mo-Ni<sub>3</sub>S<sub>4</sub>/CW samples compared to Ni<sub>3</sub>S<sub>4</sub>/CW, further confirming the lattice expansion of Ni<sub>3</sub>S<sub>4</sub> due to the Mo-doping.

Nitrogen (N<sub>2</sub>) adsorption/desorption measurement was furtherly carried out to study specific surface area and porous structure of Mo-Ni<sub>3</sub>S<sub>4</sub>/CW. As shown in Fig. 2c, the Mo-Ni<sub>3</sub>S<sub>4</sub>/CW-0.4 delivers a typical



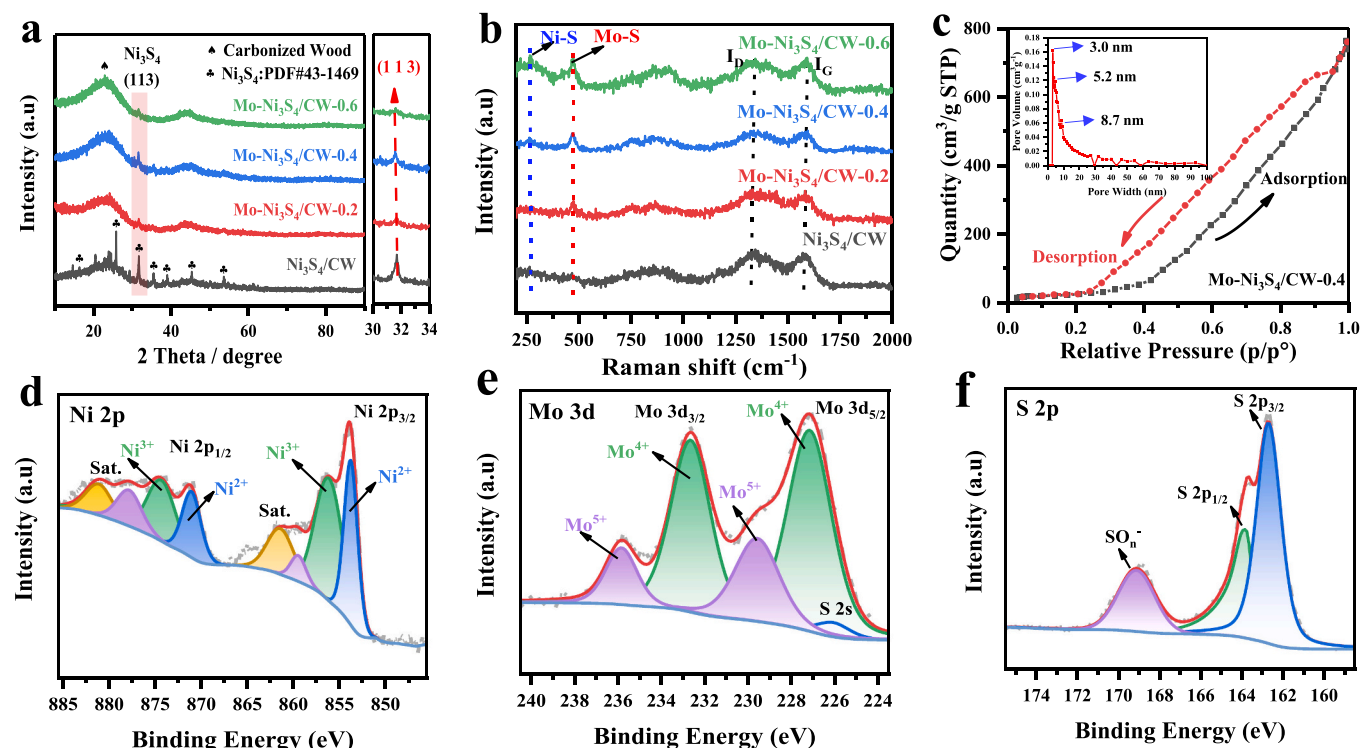


Fig. 2. (a) XRD patterns, and the right panel is the enlarged figures of the orange area. (b) Raman patterns of samples. (c)  $N_2$  adsorption/desorption isotherms and inset is the pore size distribution, and High-resolution XPS spectrum of (d) Ni 2p, (e) Mo 3d, and (f) S 2p of Mo-Ni $_3$ S $_4$ /CW-0.4.

IV isotherm with an obvious hysteresis loop [30], indicating abundant mesoporous structure existence, as supported by the pore size distribution (inset in Fig. 2c). As shown in Table S2, the specific surface area ( $S_{BET}$ ) was calculated to be  $59 \text{ m}^2 \cdot \text{g}^{-1}$  for Mo-Ni $_3$ S $_4$ /CW-0.4, which is much larger than that of Mo-Ni $_3$ S $_4$  ( $8.9 \text{ m}^2 \cdot \text{g}^{-1}$ ). In addition, the surface wettability of Mo-Ni $_3$ S $_4$ /CW-0.4 and CW samples was also evaluated by the water contact angle (CA) measurement. As shown in Fig. S11, the Mo-Ni $_3$ S $_4$ /CW-0.4 delivers the water CA of  $0^\circ$  much lower than that of CW ( $109.8^\circ$ ), showing a superhydrophilic surface of Mo-Ni $_3$ S $_4$ /CW-0.4. The droplets were promptly diffused and infiltrated once contacting the surface of Mo-Ni $_3$ S $_4$ /CW-0.4 (Video S1), suggesting its excellent surface wettability. The superhydrophilic surface, large specific surface area, and 3D low-tortuosity porous structure of Mo-Ni $_3$ S $_4$ /CW-0.4 enable the electrolyte to sufficiently permeate through whole electrode, resulting in highly exposed active sites, rapidly mass transportation, and an easily accessible solid-liquid interface, thus promoting efficient electrocatalysis for water splitting.

Supplementary material related to this article can be found online at doi:10.1016/j.apcatb.2023.123123.

As exhibited in Fig. S12a, XPS full spectrum of Mo-Ni $_3$ S $_4$ /CW-0.4 clearly reveals the presence of Ni, Mo, S, C, and O elements. The Ni 2p (Fig. 2d) delivers two peaks located at  $\sim 854.1$  and  $\sim 871.5$  eV, assigning to Ni 2p $_{3/2}$  and Ni 2p $_{1/2}$  respectively [31]. The Ni-species are presented with Ni $^{2+}$  and Ni $^{3+}$  states according to the binding energy gap of 17.4 eV between the Ni 2p $_{3/2}$  and Ni 2p $_{1/2}$ . Moreover, Mo-Ni $_3$ S $_4$ /CW-0.4 displays a molar ratio of 0.45 for the Ni $^{2+}$ /Ni $^{3+}$  (Table S3), slightly lower than that of Ni $_3$ S $_4$ /CW (0.49), indicating the Ni atom loses electron whereas Mo atom acquires electron. Therefore, there are strong electronic interactions between the Ni and Mo atoms in Mo-Ni $_3$ S $_4$ /CW-0.4. From the high-resolution XPS spectrum of Mo 3d, two obvious peaks located at  $\sim 227.2$  eV and  $\sim 232.7$  eV can be observed in Fig. 2e, which are attributed to Mo 3d $_{5/2}$  and Mo 3d $_{3/2}$ , respectively [32]. It can be deconvoluted into two couples of peaks at 227.2/229.6 eV and 232.7/235.9 eV deriving from Mo $^{4+}$  and Mo $^{5+}$ , respectively. The C 1s spectrum of Mo-Ni $_3$ S $_4$ /CW-0.4 reveals two distinct peaks located at  $\sim$

284.8 eV and  $\sim 286.3$  eV, corresponding to the C-C/C=C bond and C-O bond, respectively (Fig. S12b) [33]. For S 2p spectra (Fig. 2f), three main peaks located around  $\sim 162.8$  eV (S 2p $_{3/2}$ ),  $\sim 163.9$  eV (S 2p $_{1/2}$ ) and  $\sim 169.1$  eV are observed, which can be ascribed to the metal-sulfur bond (Mo/Ni-S), low coordination sulfur (S $^{2-}$ ), and S-O bond (SO $_n$ ), respectively [34,35]. The O 1s spectra of Mo-Ni $_3$ S $_4$ /CW-0.4 shows three distinct peaks at  $\sim 530.7$ ,  $\sim 532.2$ , and  $\sim 534.1$  eV, which are attributed to the meta-oxygen bond (Mo/Ni-O), C-O bond and adsorbed water (H-O-H) bond, respectively (Fig. S12c) [36,37].

### 3.2. Electrocatalytic hydrogen evolution reaction

The HER activity of as-synthesized catalysts was measured in the 1.0 M KOH electrolyte using typical three-electrode electrochemical cell. As shown in Fig. 3a and b, the linear sweep voltammetry (LSV) curves demonstrate that Mo-Ni $_3$ S $_4$ /CW-0.4 delivers a best HER activity, requiring only overpotentials of 17 and 270 mV for acquiring current densities ( $\eta$ ) of 10 and  $100 \text{ mA cm}^{-2}$ , superior than commercial Pt/C ( $\eta_{10} = 96 \text{ mV}$ ,  $\eta_{100} = 284 \text{ mV}$ ). This performance is much better than that of Ni $_3$ S $_4$ /CW ( $\eta_{10} = 280 \text{ mV}$ ), Mo-Ni $_3$ S $_4$ /CW-0.2 ( $\eta_{10} = 73 \text{ mV}$ ,  $\eta_{100} = 325 \text{ mV}$ ), Mo-Ni $_3$ S $_4$ /CW-0.6 ( $\eta_{10} = 33 \text{ mV}$ ,  $\eta_{100} = 309 \text{ mV}$ ), and several representative electrocatalysts reported recently (Table S5). In addition, Mo-Ni $_3$ S $_4$ /CW-0.4 also exhibited excellent performance at higher current densities; the overpotential was  $\sim 350 \text{ mV}$  for a current density of  $400 \text{ mA cm}^{-2}$ . These results suggest that the introduction of Mo plays a virtual role in the enhancement of HER activity. The Tafel slope of Mo-Ni $_3$ S $_4$ /CW-0.4 is only  $18.6 \text{ mV dec}^{-1}$  (Fig. 3c), which is lower than that of Pt/C ( $20.0 \text{ mV dec}^{-1}$ ), Mo-Ni $_3$ S $_4$ /CW-0.6 ( $31.0 \text{ mV dec}^{-1}$ ), Mo-Ni $_3$ S $_4$ /CW-0.2 ( $41.2 \text{ mV dec}^{-1}$ ), and Ni $_3$ S $_4$ /CW ( $122 \text{ mV dec}^{-1}$ ) indicating excellent HER kinetics for the Mo-Ni $_3$ S $_4$ /CW-0.4 [38]. Electrochemical impedance spectroscopy (EIS) was also used to investigate the electrode kinetics (Fig. 3d). Obviously, Mo-Ni $_3$ S $_4$ /CW-0.4 exhibits a smallest charge transfer resistance value of  $74.8 \Omega$  than Ni $_3$ S $_4$ /CW ( $187.0 \Omega$ ), Mo-Ni $_3$ S $_4$ /CW-0.2 ( $76.7 \Omega$ ), and Mo-Ni $_3$ S $_4$ /CW-0.6 ( $120 \Omega$ ), implying faster charge transfer kinetics promoted by Mo

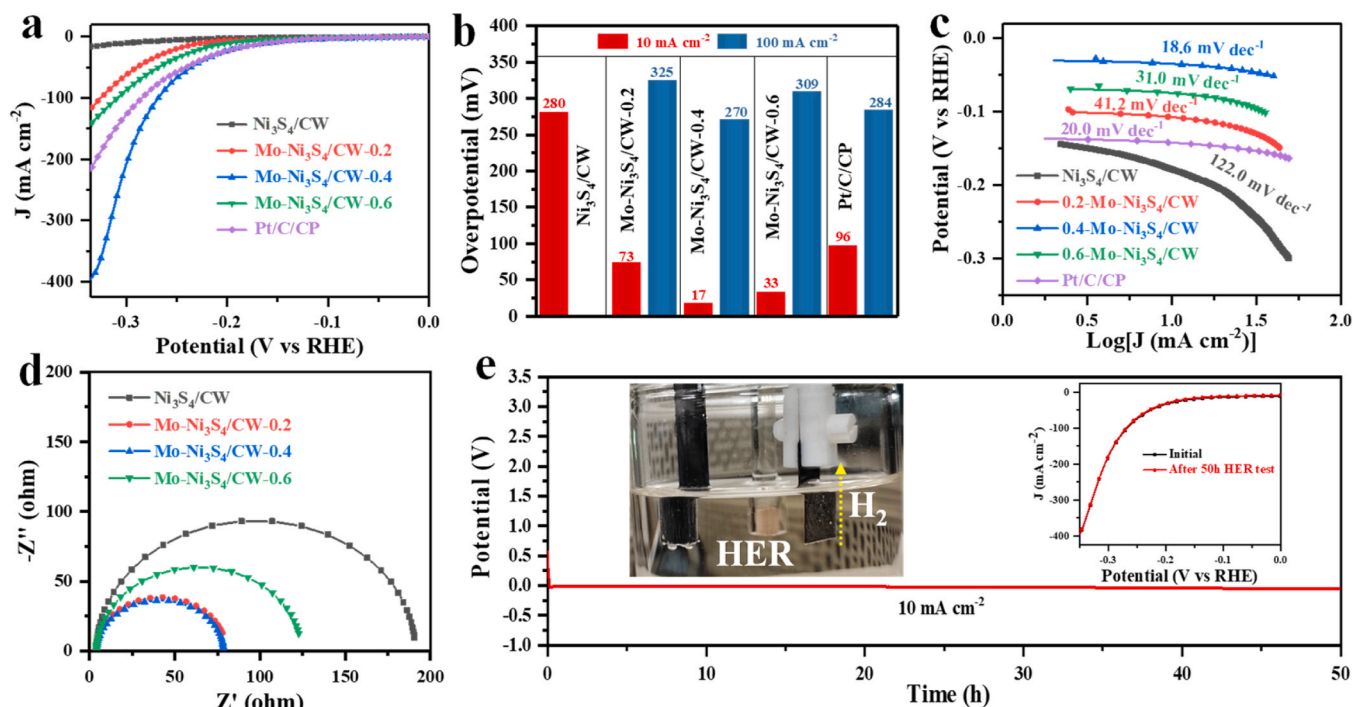


**Fig. 3.** (a) iR-Corrected polarization curves, (b) Corresponding overpotential histograms at 10 and 100  $\text{mA cm}^{-2}$ , (c) Tafel plots, and (d) Nyquist plots of different catalysts. (e) Long-term stability of  $\text{Mo-Ni}_3\text{S}_4/\text{CW-0.4}$  at 10  $\text{mA cm}^{-2}$  in 1.0 M KOH solution. Insets are HER device with  $\text{Mo-Ni}_3\text{S}_4/\text{CW-0.4}$  electrode and LSV curves initial and after HER test.

incorporation [39]. This can be attributed to the lattice expansion of  $\text{Ni}_3\text{S}_4$  that results in redistribution of surface electronic states, which facilitates the transfer of surface/interface electrons and thus reduces the reaction energy barrier of HER.

Further, the long-term stability of  $\text{Mo-Ni}_3\text{S}_4/\text{CW-0.4}$  was also

measured by the V-t chronoamperometric tests and CV cycles and (Fig. 3e). Both polarization curves and V-t chronoamperometric tests of  $\text{Mo-Ni}_3\text{S}_4/\text{CW-0.4}$  present a negligible voltage degradation after continuous 50 h electrocatalysis at 10  $\text{mA cm}^{-2}$ . These results demonstrate that the  $\text{Mo-Ni}_3\text{S}_4/\text{CW-0.4}$  catalyst has superior HER durability.

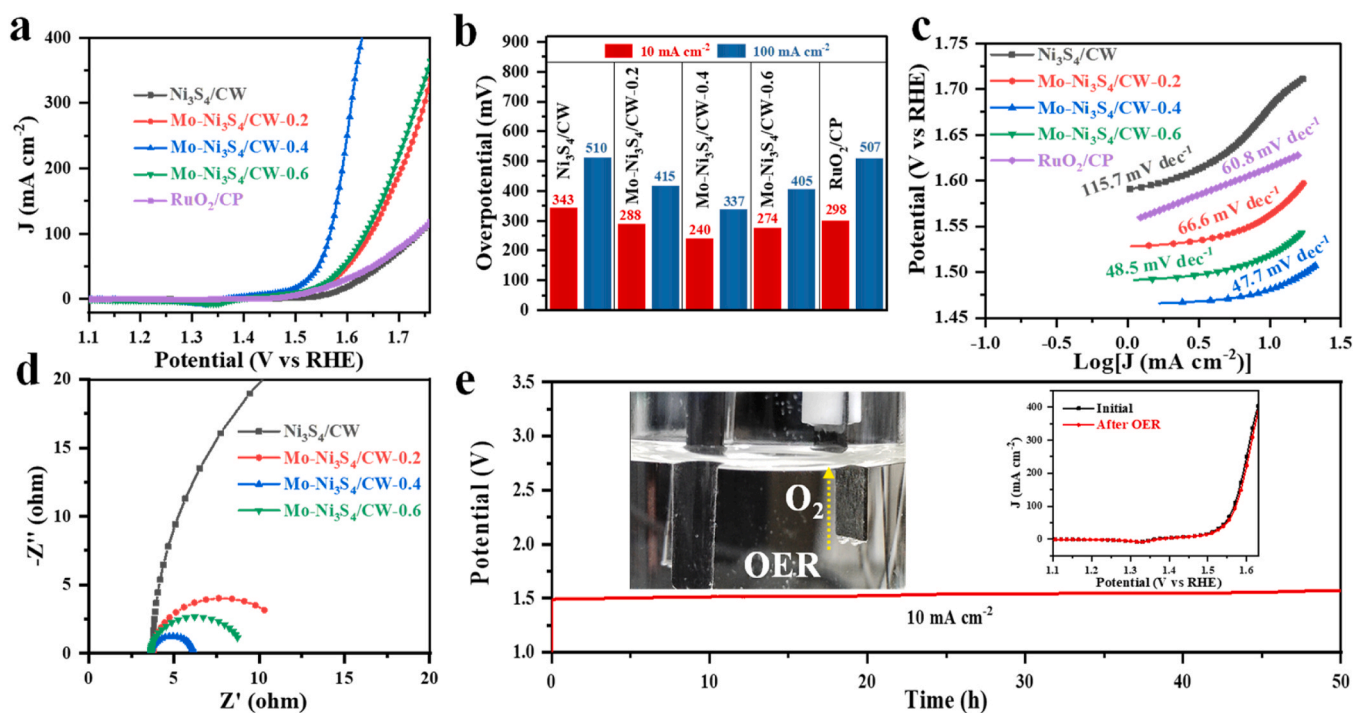


**Fig. 4.** (a) iR-Corrected LSV curves, (b) Corresponding overpotential histograms at 10 and 100  $\text{mA cm}^{-2}$ , (c) Tafel plots, and (d) Nyquist plots of different catalysts. (e) Long-term stability of  $\text{Mo-Ni}_3\text{S}_4/\text{CW-0.4}$  at 10  $\text{mA cm}^{-2}$  in 1.0 M KOH solution. Insets are OER device with  $\text{Mo-Ni}_3\text{S}_4/\text{CW-0.4}$  electrode and LSV curves of initial and after OER test.

The composition and structure of the Mo-Ni<sub>3</sub>S<sub>4</sub>/CW-0.4 catalyst after electrocatalytic HER measurements were further characterized. As seen from the SEM images shown in Fig. S18, the Mo-Ni<sub>3</sub>S<sub>4</sub>/CW-0.4 still retained a 3D network structure of wooden carbon, except that slightly aggregation of small nanosheets. Further, both the XRD and Raman spectra (Fig. S19a, b) also reveal no significant change is found for the Mo-Ni<sub>3</sub>S<sub>4</sub>/CW-0.4 after 50 h HER test, indicating Mo-Ni<sub>3</sub>S<sub>4</sub>/CW-0.4 retains its initial componential, morphological, and structural integrity during HER electrolysis. After 50 h electrolysis, the ratio of Ni<sup>2+</sup>/Ni<sup>3+</sup> in Mo-Ni<sub>3</sub>S<sub>4</sub>/CW-0.4 is 0.41, lower than that of the initial Mo-Ni<sub>3</sub>S<sub>4</sub>/CW-0.4 (Ni<sup>2+</sup>/Ni<sup>3+</sup> = 0.45), indicating Ni atom loses electron during the HER process (Fig. S20b, and Table S3). Meanwhile, the Mo atom acquires electron, leading to the ratio decrease of Mo<sup>5+</sup>/Mo<sup>4+</sup> of Mo-Ni<sub>3</sub>S<sub>4</sub>/CW-0.4 after HER test (Fig. S20c). The above results indicate that there are strong electronic interactions between Ni and Mo atoms (electrons transfer from Ni to Mo), which promotes the catalysis progress of HER.

### 3.3. Electrocatalytic oxygen evolution reaction

The OER electrocatalytic activities of as-synthesized catalysts were also measured. As shown in Fig. 4a, Mo-Ni<sub>3</sub>S<sub>4</sub>/CW-0.4 exhibits the overpotentials of 240 and 337 mV to reach current densities of 10 and 100 mA cm<sup>-2</sup> respectively, which are better than those of Ni<sub>3</sub>S<sub>4</sub>/CW ( $\eta_{10}$  = 343 mV,  $\eta_{100}$  = 510 mV), Mo-Ni<sub>3</sub>S<sub>4</sub>/CW-0.2 ( $\eta_{10}$  = 288 mV,  $\eta_{100}$  = 415 mV), Mo-Ni<sub>3</sub>S<sub>4</sub>/CW-0.6 ( $\eta_{10}$  = 274 mV,  $\eta_{100}$  = 405 mV), and several representative electrocatalysts reported recently (Table S6) as

well as RuO<sub>2</sub> ( $\eta_{10}$  = 298 mV,  $\eta_{100}$  = 507 mV). These results suggest that the Mo-Ni<sub>3</sub>S<sub>4</sub>/CW-0.4 has an outstanding OER performance. The Mo-Ni<sub>3</sub>S<sub>4</sub>/CW-0.4 also exhibits the lowest Tafel slope of 47.7 mV dec<sup>-1</sup> compared with Mo-Ni<sub>3</sub>S<sub>4</sub>/CW-0.6 (48.5 mV dec<sup>-1</sup>), Mo-Ni<sub>3</sub>S<sub>4</sub>/CW-0.2 (66.6 mV dec<sup>-1</sup>), and Ni<sub>3</sub>S<sub>4</sub>/CW (115.7 mV dec<sup>-1</sup>), as well as RuO<sub>2</sub> (66.6 mV dec<sup>-1</sup>) illustrating the optimum OER kinetics. Moreover, the Mo-Ni<sub>3</sub>S<sub>4</sub>/CW-0.4 delivers a smaller  $R_{ct}$  of 2.5  $\Omega$  than those of Ni<sub>3</sub>S<sub>4</sub>/CW (69.2  $\Omega$ ), Mo-Ni<sub>3</sub>S<sub>4</sub>/CW-0.2 (8.0  $\Omega$ ), and Mo-Ni<sub>3</sub>S<sub>4</sub>/CW-0.6 (5.3  $\Omega$ ), manifesting the improved OER kinetics mainly caused by Mo introduction. Additionally, the Mo-Ni<sub>3</sub>S<sub>4</sub>/CW-0.4 has a larger ECSA of 166 cm<sup>2</sup> than those of Ni<sub>3</sub>S<sub>4</sub>/CW (72.2 cm<sup>2</sup>), Mo-Ni<sub>3</sub>S<sub>4</sub>/CW-0.2 (141 cm<sup>2</sup>), and Mo-Ni<sub>3</sub>S<sub>4</sub>/CW-0.6 (94.5 cm<sup>2</sup>), meaning larger exposure of active sites in the Mo-Ni<sub>3</sub>S<sub>4</sub>/CW-0.4 (Fig. S16) [40]. While, the Mo-Ni<sub>3</sub>S<sub>4</sub>/CW-0.4 shows no obvious activity loss after CV cycles and V-t chronoamperometric tests for 50 h (Fig. 5d), suggesting its superior OER durability.

It should be noted that the growth of Mo-Ni<sub>3</sub>S<sub>4</sub> on carbon paper was also prepared (Mo-Ni<sub>3</sub>S<sub>4</sub>/CP) by the same synthetic process as Mo-Ni<sub>3</sub>S<sub>4</sub>/CW and further compared their catalytic performance. As shown in Fig. S21a and b, the overpotentials of Mo-Ni<sub>3</sub>S<sub>4</sub>/CP-0.4 are 0.294 and 1.648 V at 50 mA cm<sup>-2</sup> for HER and OER, respectively, which are both larger than Mo-Ni<sub>3</sub>S<sub>4</sub>/CW-0.4 (0.236 and 1.544 V), indicating that using naturally-hierarchical carbonized wood as electrocatalyst support can significantly improve the electrocatalytic activity of Mo-Ni<sub>3</sub>S<sub>4</sub>/CW for overall water electrolysis. Undoubtedly, the oriented microchannels in wood make Ni<sub>3</sub>S<sub>4</sub> grow orderly, allow electrolyte to fully penetrate the catalyst, and enable the generated gas products to be released quickly, which will promote the ion/mass transfer. Meanwhile, the Mo-doped

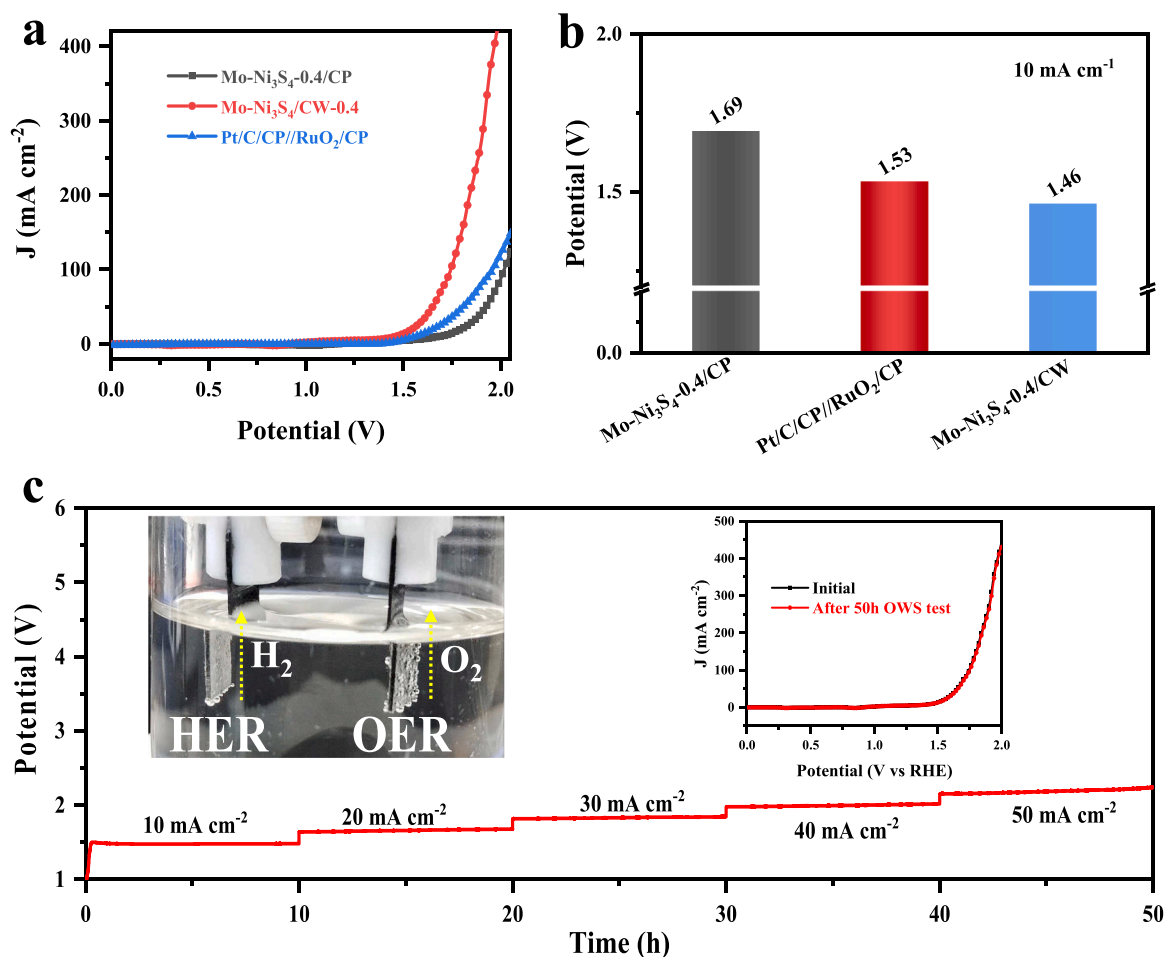


**Fig. 5.** (a) LSV of the Mo-Ni<sub>3</sub>S<sub>4</sub>-0.4/CP//Mo-Ni<sub>3</sub>S<sub>4</sub>-0.4/CP, Mo-Ni<sub>3</sub>S<sub>4</sub>/CW-0.4//Mo-Ni<sub>3</sub>S<sub>4</sub>/CW-0.4, and Pt/C/CP//RuO<sub>2</sub>/CP electrodes in 1.0 M KOH. (b) Comparison of different catalysts for OWS at 10 mA cm<sup>-2</sup>. (c) Long-term stability of Mo-Ni<sub>3</sub>S<sub>4</sub>/CW-0.4 at different current densities for 50 h. Insets are LSV curves of initial and after OWS test, and electrolysis water device with Mo-Ni<sub>3</sub>S<sub>4</sub>/CW-0.4 electrodes.



$\text{Ni}_3\text{S}_4$  is filled in various pore structures of carbonized wood, which increases the conductivity of catalyst. However, the Mo-doped  $\text{Ni}_3\text{S}_4$  tends to agglomerate and distribute unevenly on the carbon paper for the Mo- $\text{Ni}_3\text{S}_4$ /CP-0.4 catalyst (Fig. S21c), which leads to the obstruction of electron transfer and electrolyte diffusion, thus limiting their catalytic performance.

To explore the excellent activity and stability of Mo- $\text{Ni}_3\text{S}_4$ /CW-0.4 for OER, the post-OER characterizations were performed. The SEM images shows that the wooden framework structure of Mo- $\text{Ni}_3\text{S}_4$ /CW-0.4 is basically retained. However, the Mo-doped  $\text{Ni}_3\text{S}_4$  nanosheets become rougher and larger, implying probable occurrence of the new phase on the surface of Mo- $\text{Ni}_3\text{S}_4$  after OER electrocatalysis (Fig. S22). As shown in Fig. S19c, the Mo- $\text{Ni}_3\text{S}_4$ /CW-0.4 after OER shows some new diffraction peaks around  $12.8^\circ$ ,  $37.9^\circ$ ,  $50.1^\circ$ ,  $66.1^\circ$ , and  $68.4^\circ$ , which can be assigned to the (003), (102), (108), (110), and (001) planes of nickel oxyhydroxide (Ni-OOH, PDF#06-0075), respectively [41]. While, the XRD also displays the disappearance of diffraction peak of (113) plane for  $\text{Ni}_3\text{S}_4$  probably due to the generation of Ni-OOH on the Mo- $\text{Ni}_3\text{S}_4$ /CW-0.4. As shown in Fig. S19d, two obvious peaks located at  $\sim 436.1\text{ cm}^{-1}$  and  $\sim 595.6\text{ cm}^{-1}$  are attributed to the characteristic signals of Ni-OOH [42], further indicating the surface of Mo- $\text{Ni}_3\text{S}_4$ /CW-0.4 should be partially oxidized into the Ni-OOH during the OER process. In addition, the XPS Ni2p spectra demonstrates the ratio of  $\text{Ni}^{2+}/\text{Ni}^{3+}$  is decreased from 0.45 to 0.22, suggesting the  $\text{Ni}^{3+}$  content is increased (Fig. S23b). However, the ratio of  $\text{Mo}^{4+}/\text{Mo}^{5+}$  is increased from 2.87 to 2.98, indicating the Mo acquires electron (Fig. S23c and Table S3). According to ICP result, Table S4 showed that a very minor amount of

Mo was detected during the whole process of OER. While a little Ni was etched from the surface of the material after OER, which agrees with the fact that Ni-OOH species were formed on the surface. The main peak for S 2p was almost disappeared (Fig. S23d), which could be attributed to the formation of Ni-OOH species on the surface of Mo- $\text{Ni}_3\text{S}_4$ /CW-0.4 and leaching of a few sulfides species after OER. For the O1s spectra (Fig. S23e), there is a new peak appeared, which is assigned to the nickel-oxygen (Ni-O) bond deriving from the Ni-OOH [36], again confirming the generation of Ni-OOH during the OER process. The above results demonstrate that there are strong electronic interactions between Ni and Mo atoms, and the generation of Ni-OOH species, which significantly facilitate the OER process [43].

### 3.4. Overall water splitting performance

The Mo- $\text{Ni}_3\text{S}_4$ /CW-0.4 was further used as a bifunctional electrocatalyst to investigate the overall water splitting (OWS) in a two-electrode system with the KOH (1 M) electrolyte. As shown in Fig. 5a and b, the electrolyzer assembled using two identical Mo- $\text{Ni}_3\text{S}_4$ /CW-0.4 electrodes needs only a small cell voltage of 1.46 V attain  $10\text{ mA cm}^{-2}$ , lower than those of Mo- $\text{Ni}_3\text{S}_4$ /CP//Mo- $\text{Ni}_3\text{S}_4$ /CP (1.69 V), Pt-C/CP//RuO<sub>2</sub>/CP (1.56 V), and most of the reported bifunctional electrocatalysts (Table S7). It should be noted that the electrolyzer based on Mo- $\text{Ni}_3\text{S}_4$ /CP catalysts needs 23 mV more than that of the Mo- $\text{Ni}_3\text{S}_4$ /CW-0.4 catalysts, unambiguously indicating the great significance of low-tortuosity hierarchically porous CW substrate comparing carbon paper (CP) during the OWS process. Additionally, the electrolyzer also

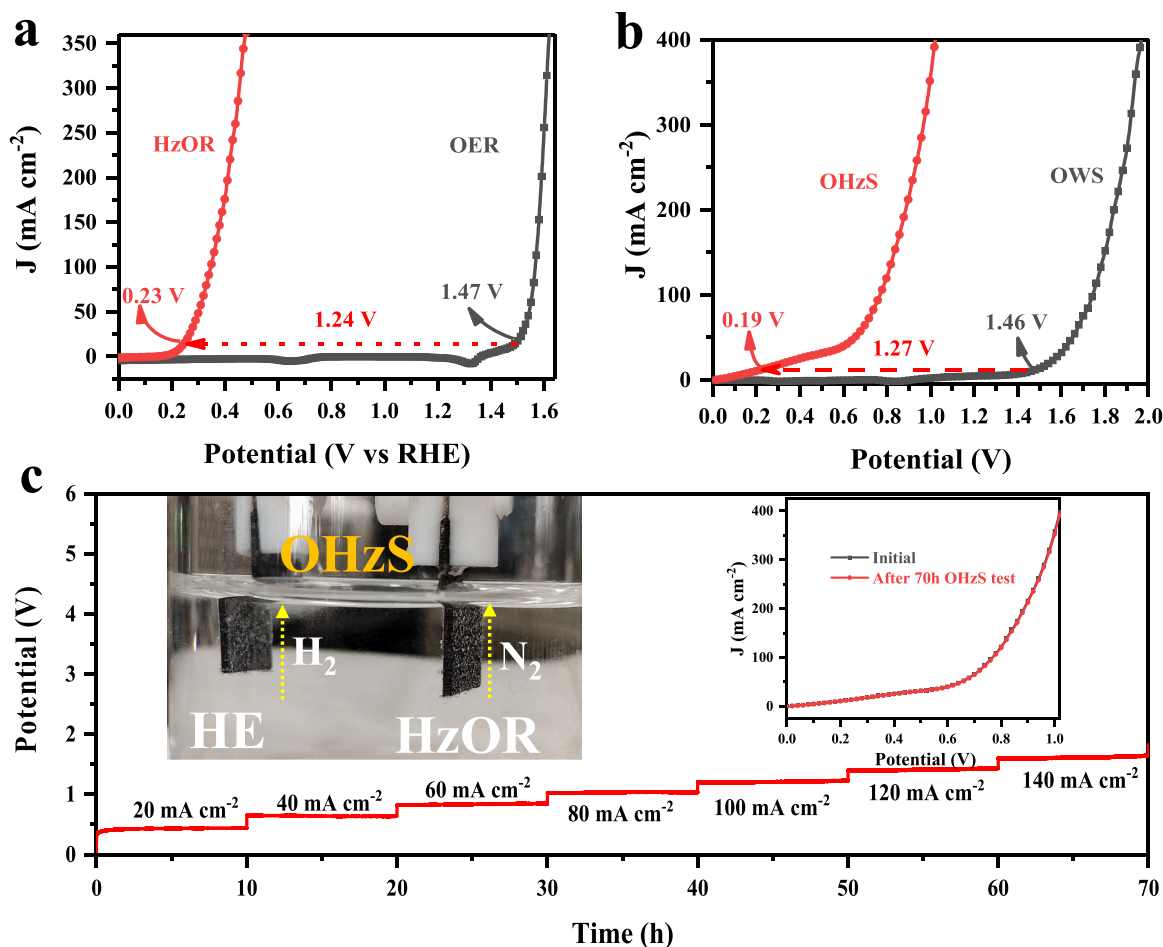


**Fig. 6.** (a) LSV curves of OER and HzOR, (b) LSV curves of OHzS and OWS for Mo- $\text{Ni}_3\text{S}_4$ /CW-0.4 with and without the addition of 0.5 M  $\text{N}_2\text{H}_4$  in 1.0 M KOH, respectively. (c) Long-term stability of Mo- $\text{Ni}_3\text{S}_4$ /CW-0.4 at different current densities for 70 h. Insets are LSV curves of initial and after OHzS test, and the corresponding electrolysis device with Mo- $\text{Ni}_3\text{S}_4$ /CW-0.4 electrode.

exhibits excellent stability without obvious potential decay after continuous operation at different current densities from 10 to 50 mA cm<sup>-2</sup> for 50 h (Fig. 5c). Large amounts of H<sub>2</sub> and O<sub>2</sub> gas were generated on the surface of the cathode and the anode, respectively (Video S2). More impressively, only an ultralow voltage of 0.19 V was required to draw a current density of 10 mA cm<sup>-2</sup> for hydrazine oxidation-assisted water electrolysis (Fig. 6a and b), which is significantly lower than that of conventional OWS ( $\eta_{10} = 1.46$  V). Abundant bubbles (H<sub>2</sub> and N<sub>2</sub>) are produced on the surface of cathode and anode electrodes under a cell voltage of 0.19 V, respectively (Video S3). Moreover, no remarkable voltages change is observed after continuous electrolysis for 70 h at different current densities (from 20 to 140 mA cm<sup>-2</sup>), which further confirms the robust durability of Mo-Ni<sub>3</sub>S<sub>4</sub>/CW-0.4 (Fig. 6c). As shown in Fig. S24, the Faraday efficiency (FE) of OWS was measured via comparing the ratio of actual H<sub>2</sub> and O<sub>2</sub> production in the H-type electrolytic cell. Notably, the amount of evolved H<sub>2</sub> and O<sub>2</sub> production could meet the theoretical hydrogen production, which suggested that the FE was nearly 100%. Similarly, the Mo-Ni<sub>3</sub>S<sub>4</sub>/CW-0.4 exhibited a high conversion of 99.97% in electrocatalytic HzOR and nearly 100% FE (Fig. S25).

Supplementary material related to this article can be found online at doi:10.1016/j.apcatb.2023.123123.

### 3.5. Study of catalytic mechanism

The chemical microenvironment of Mo-Ni<sub>3</sub>S<sub>4</sub>/CW-0.4 was further investigated using in situ Raman spectroscopy (Fig. 7). As shown in Fig. 7a-c, two prominent peaks at 290.6 and 471.4 cm<sup>-1</sup> are assigned to Ni-S and Mo-S vibrations [44], respectively. The relative intensity of the two peaks increased as the potential was changed from 0 to -1.2 V. This result suggests that Mo atoms replace partial Ni and intercalate into the lattice of Ni<sub>3</sub>S<sub>4</sub>, leading to an enlarged lattice distance and strong electronic interactions, thereby facilitating the catalytic HER. For the OER process (Fig. 7d-f), as the potentials was increased, the relative intensity of two signal peaks at ~436.1 and ~595.6 cm<sup>-1</sup> increased, which are assigned to the Ni-OOH vibrations [45]. Moreover, the Mo-Ni<sub>3</sub>S<sub>4</sub>/CW-0.4 displays a lower voltage of 0.4 V (Fig. 7f) for formation of Ni-OOH than those of Ni<sub>3</sub>S<sub>4</sub>/CW (1.2 V), Mo-Ni<sub>3</sub>S<sub>4</sub>/CW-0.2 (0.8 V), and Mo-Ni<sub>3</sub>S<sub>4</sub>/CW-0.6 (0.6 V) respectively (Fig. S26), indicating that an optimal amount of Mo-doping is favorable to the generation of Ni-OOH species. The formation of Ni-OOH species is attributed to the increase of the oxidation state of Ni caused by the Mo intercalation, which is considered as main active sites for OER (Fig. 7g). Further, electron paramagnetic resonance (EPR) was employed to detect the surface defects of the Mo-Ni<sub>3</sub>S<sub>4</sub>/CW-0.4 before and after OER. As shown in Fig. S27, the Mo-Ni<sub>3</sub>S<sub>4</sub>/CW-0.4 had a strong sulfur defect peak at g

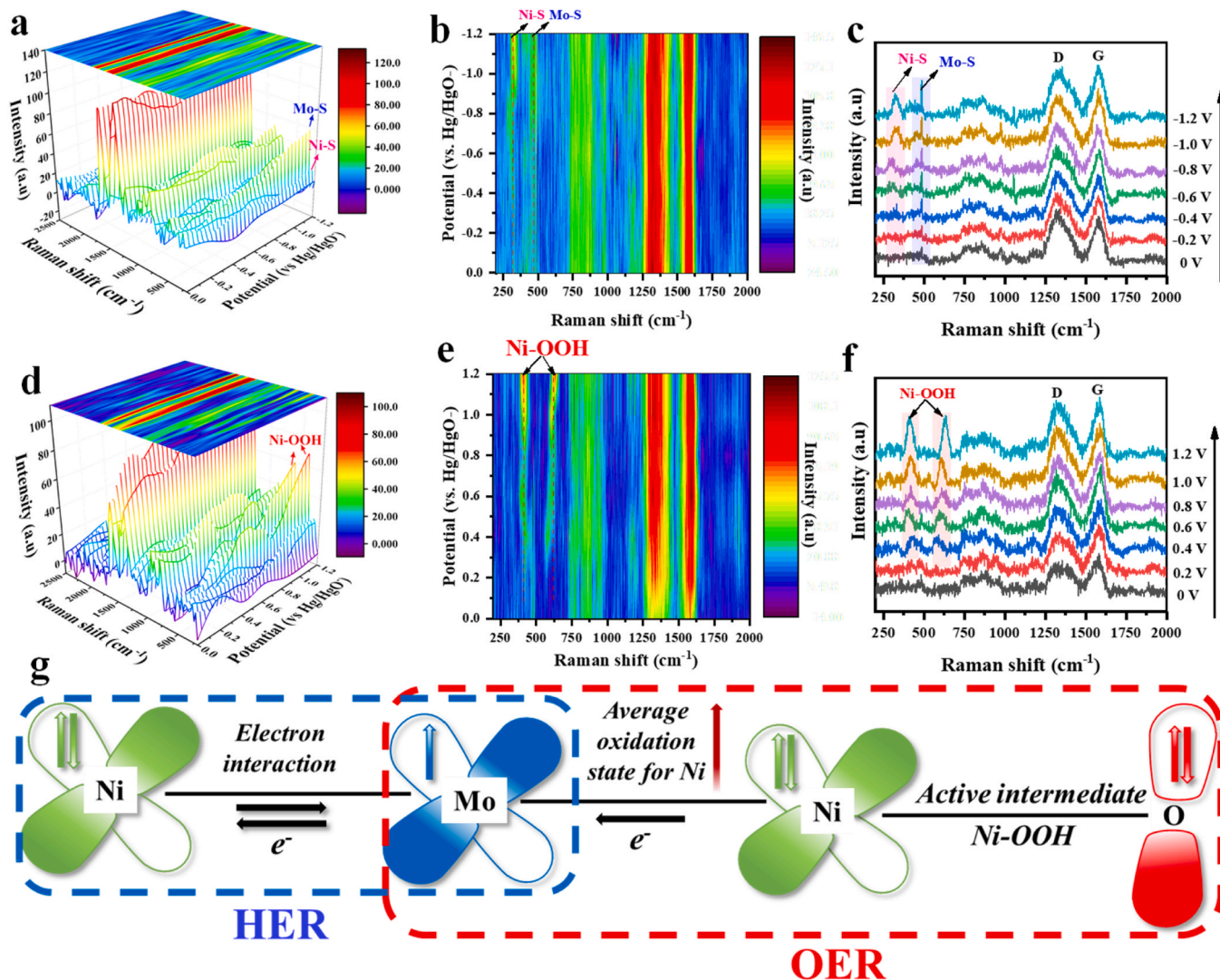


Fig. 7. In situ Raman spectra of Mo-Ni<sub>3</sub>S<sub>4</sub>/CW-0.4 during the HER (a-c) and OER (d-f) process. (a, d) 3D and (b, e) 2D mapping images, and (c, f) in situ Raman spectra at different voltages from 0 to -1.2 V vs. Hg/HgO. (g) Schematic illustration of the electronic coupling between Mo and Ni.

= 2.004, indicating the S-vacancies formation in the Mo-Ni<sub>3</sub>S<sub>4</sub>/CW-0.4 after OER [46], which is consistent with the result of ICP (Table S4). Therefore, the dissolution of Ni species and self-reconstruction during the OER, as well as the formation of S-vacancies should be the main factors for enhancement of OER activity. Similar phenomenon was also obtained by the previous work [47]. Additionally, the two signals appeared around 1324 (D signal) and 1584 cm<sup>-1</sup> (G signal) are unchanged [48], suggesting the microstructural feature of CW remained unchanged during both HER and OER processes.

DFT-based calculations were used to gain some insight for the improved performance of the OER and HER. The optimized models of Ni<sub>3</sub>S<sub>4</sub> and Mo-Ni<sub>3</sub>S<sub>4</sub> were established (Fig. 8a). As shown in Fig. 8b, the Mo-Ni<sub>3</sub>S<sub>4</sub> exhibits a similar energy band structure with Ni<sub>3</sub>S<sub>4</sub>, indicating that the introduction of Mo does not change the metal-like property of Ni<sub>3</sub>S<sub>4</sub>. In addition, the total density of states (TDOS) of Ni<sub>3</sub>S<sub>4</sub> and Mo-Ni<sub>3</sub>S<sub>4</sub> were calculated (Fig. 8c). Compared with Ni<sub>3</sub>S<sub>4</sub>, the TDOS of Mo-Ni<sub>3</sub>S<sub>4</sub> delivers a higher density of electronic cloud near Fermi level, attributed to lattice expansion of the Ni<sub>3</sub>S<sub>4</sub> by Mo-doping. The enhanced TDOS is beneficial to reduce the reaction energy barrier of water splitting [49], thereby improving the catalytic activity. Moreover, the partial total density of states (PDOS) of Ni<sub>3</sub>S<sub>4</sub> and Mo-Ni<sub>3</sub>S<sub>4</sub> were also calculated to further investigate the role of Mo-doping (Fig. 8d). Clearly, there is no obvious change for the PDOS of Ni and S in both the Ni<sub>3</sub>S<sub>4</sub> and Mo-Ni<sub>3</sub>S<sub>4</sub>, which indicates that the increased TDOS of Mo-Ni<sub>3</sub>S<sub>4</sub> originates from the Mo-incorporation. As shown in Fig. 9a, the charge density around Mo atom (blue) is obviously increased, while the Ni atom (yellow) decreased. This result indicates that the introduction of Mo not only leads to lattice expansion of Ni<sub>3</sub>S<sub>4</sub>, but also regulates the surface local electronic density state of Mo-Ni<sub>3</sub>S<sub>4</sub>/CW. The energy barrier of H<sub>2</sub>O dissociation on the Mo-Ni<sub>3</sub>S<sub>4</sub> was calculated to be 0.65 eV, lower than that of Ni<sub>3</sub>S<sub>4</sub> (1.28 eV) indicating that the introduction of Mo

significantly reduces the water dissociation energy (Fig. 9b). Besides, the effect of Mo-doping on hydrogen adsorption Gibbs free energy ( $\Delta G_{H^*}$ ) was also investigated. The  $\Delta G_{H^*}$  is closer to zero represents better HER activity [50]. Mo-Ni<sub>3</sub>S<sub>4</sub> delivers a much smaller  $\Delta G_{H^*}$  of 0.08 eV than Ni<sub>3</sub>S<sub>4</sub> (0.25 eV), indicating Mo-Ni<sub>3</sub>S<sub>4</sub> has a higher catalytic activity for HER. Compared to Ni sites in Ni<sub>3</sub>S<sub>4</sub>, that of Mo-Ni<sub>3</sub>S<sub>4</sub> shows the lower  $\Delta G_{H^*}$  and energy barrier of water dissociation (Fig. 9b and c), indicating that the introduction of Mo favors to improving the intrinsic catalytic activity of Ni sites in Mo-Ni<sub>3</sub>S<sub>4</sub>. Additionally, the generation of Nickel (oxy)hydroxide species (Ni-OOH) on Mo-Ni<sub>3</sub>S<sub>4</sub> surface are regarded as real active species for OER, as supported by some recent works [47,51–53]. In alkaline environment, a possible OER mechanism is proposed by a four-electron transfer process (Fig. 9d) [54]. Moreover, the reaction free energy barrier of Mo-Ni<sub>3</sub>S<sub>4</sub> and Ni-OOH was calculated, according to the four-electron route of OER. Fig. 9e shows that the step of deprotonation of OH\* to O\* is the rate-determined step (RDS). The reaction barrier of Ni-OOH is 1.71 eV for the O\* formation, lower than that of Mo-Ni<sub>3</sub>S<sub>4</sub> (1.90 eV), indicating Ni-OOH has a better OER activity compared to Mo-Ni<sub>3</sub>S<sub>4</sub>. Further, the d-band center of Ni in Ni-OOH (−1.90 eV) is closer to the Fermi level in comparison with Mo-Ni<sub>3</sub>S<sub>4</sub> (−2.08 eV), indicating the Ni site of Ni-OOH has higher valence states and more antibonding states, thereby favoring the OER performance (Fig. 9f). The generated Ni-OOH layer on the Mo-doped Ni<sub>3</sub>S<sub>4</sub> can reduce the energy barrier of O-H bond breakage in H<sub>2</sub>O, increasing the kinetics of OER and boosting the O<sub>2</sub> production. Thus, above theoretical calculations very well verify experimental results. Additionally, the Mo-Ni<sub>3</sub>S<sub>4</sub>/CW-0.4 still maintains a highly hydrophilic surface after HER and OER tests (Fig. S28).

In short, the outstanding electrocatalytic activity of Mo-Ni<sub>3</sub>S<sub>4</sub>/CW-0.4 can be mainly attributed to its unique architecture and the synergistic effect of electronic structure and Mo-doping. i) The unique 3D low-

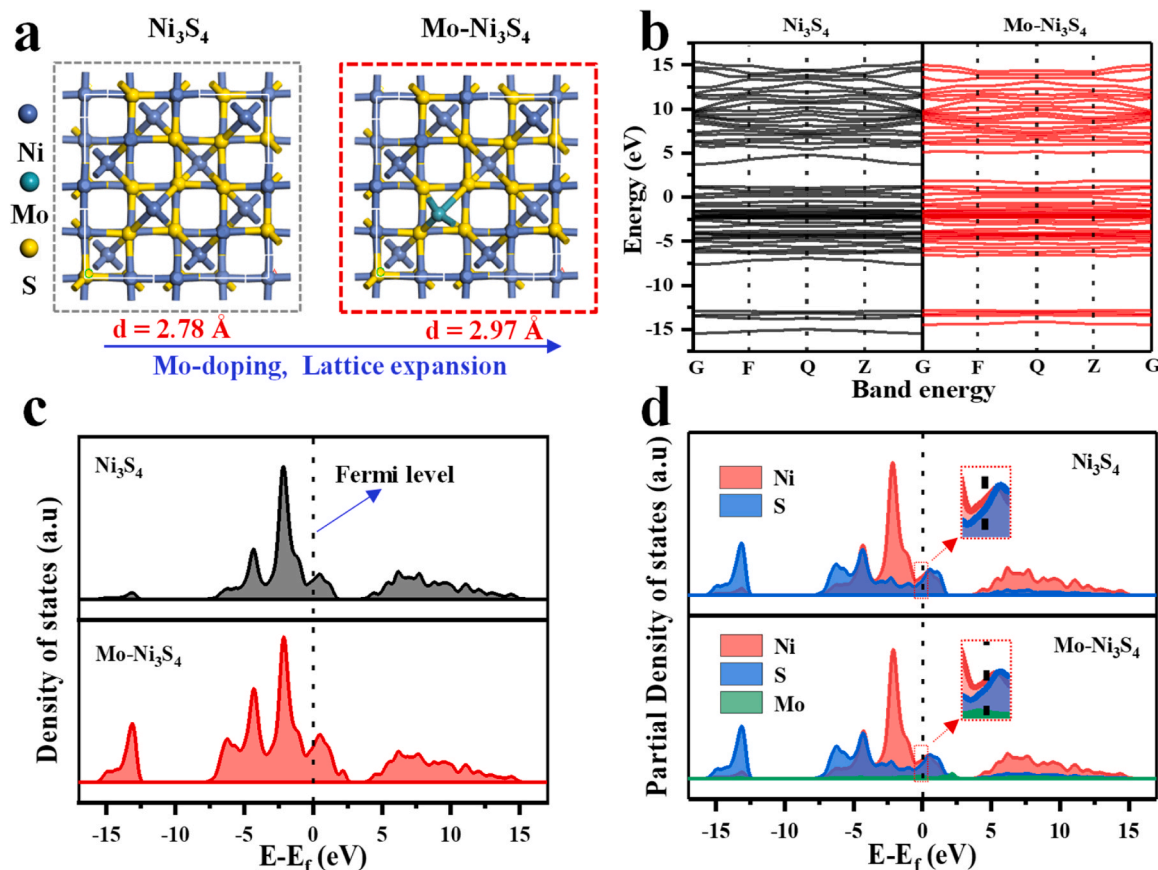
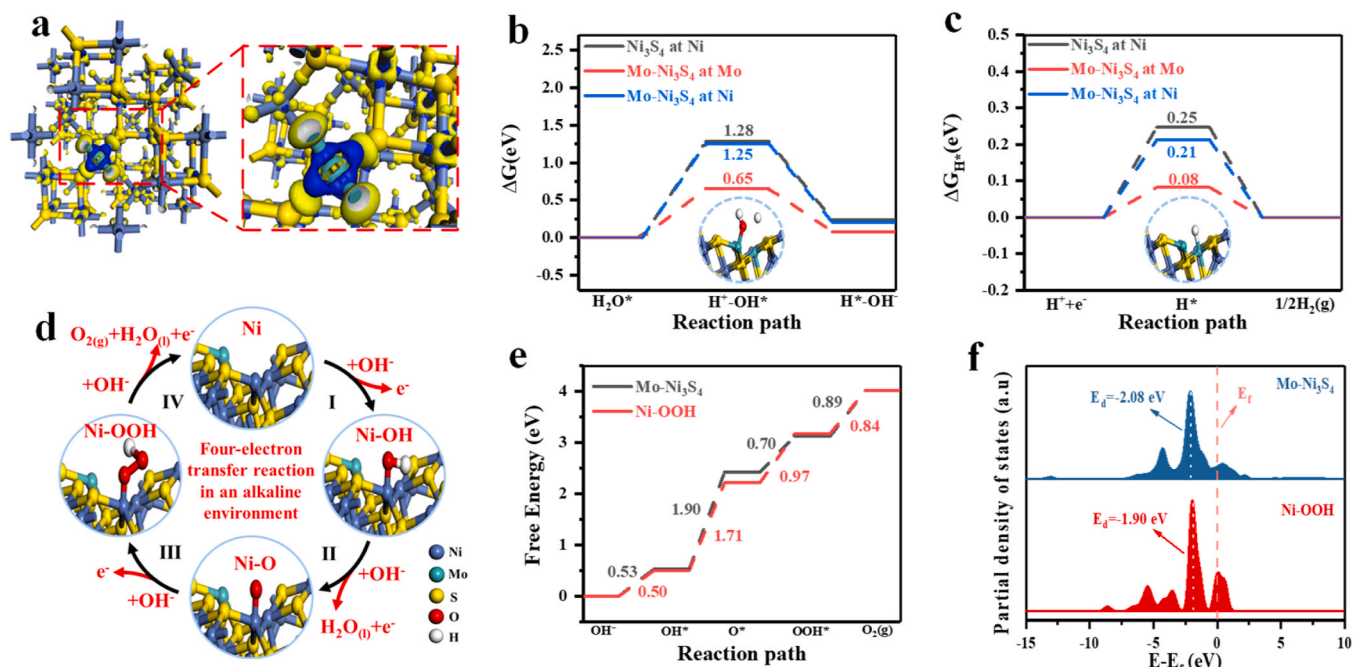


Fig. 8. (a) Structural models, (b) calculated energy band, (c) total density of states, and (d) partial density of states of Ni<sub>3</sub>S<sub>4</sub> and Mo-Ni<sub>3</sub>S<sub>4</sub>, respectively.





**Fig. 9.** (a) Charge density of Mo-Ni<sub>3</sub>S<sub>4</sub>. (b) Energy barriers of water dissociation and (c)  $\Delta G_{H^+}$  for Ni<sub>3</sub>S<sub>4</sub> and Mo-Ni<sub>3</sub>S<sub>4</sub>. (d) possible OER mechanism. (e) Free energy diagrams (f) Ni d-band center of Mo-Ni<sub>3</sub>S<sub>4</sub> and Ni-OOH for OER. The Ni, Mo, and S atoms are represented with blue, cyan, and yellow spheres, respectively.

tortuosity hierarchically porous structure is beneficial to the infiltration of electrolyte, exposure of more active sites, and the release of gaseous products. In addition, the high electrical conductivity and low energy barrier for the H adsorption of Mo-Ni<sub>3</sub>S<sub>4</sub>/CW-0.4 promote the HER process. ii) The Mo incorporated Ni<sub>3</sub>S<sub>4</sub> with lattice expansion can regulate the electronic structure of active sites and facilitate the adsorption of H/O-containing species. While, the formation of Ni-OOH on the Mo-Ni<sub>3</sub>S<sub>4</sub> @CW-0.4 favors to improving the intrinsic activity of OER. iii) The strong coordination interaction between the Mo-Ni<sub>3</sub>S<sub>4</sub> and CW can provide rapid charge collection, short transmission distance of mass, and good structural stability. Thus, these features of Mo-Ni<sub>3</sub>S<sub>4</sub> @CW-0.4 catalyst endow to its outstanding OWS performance in the alkaline medium, making it highly attractive candidates for practical industrial application.

#### 4. Conclusions

In summary, 3D low-tortuosity porous CW supported Mo-incorporated Ni<sub>3</sub>S<sub>4</sub> nanosheets with lattice expansion as a highly efficient bifunctional electrocatalyst for OWS has been developed. The lattice expansion of Ni<sub>3</sub>S<sub>4</sub> by Mo incorporation regulates the local electronic structure and optimizes the adsorption energy of hydrogen/oxygen species, thus promoting electrocatalytic performance of HER and OER. Additionally, the Ni-OOH layer formed through surface reconstruction of Ni<sub>3</sub>S<sub>4</sub> boosted by Mo-doping, which significantly enhances the intrinsic activity for OER. Furthermore, the 3D low-tortuosity porous structure derived from natural wood enhances the exposure of abundant active sites, and offers tri-phase pathways for rapid transport of ions, electrons, and gaseous species involved in the electrode processes. Therefore, the Mo-Ni<sub>3</sub>S<sub>4</sub>/CW-0.4 catalyst exhibits ultralow overpotentials of 17 and 240 mV to achieve a current density of 10 mA cm<sup>-2</sup> for HER and OER, respectively. Besides, an electrolyzer composed of Mo-Ni<sub>3</sub>S<sub>4</sub>/CW-0.4 electrode demonstrates a low cell voltage of 1.46 V for OWS to achieve 10 mA cm<sup>-2</sup> while maintaining excellent cycle durability. More impressively, the electrolyzer requires only an ultralow voltage of 0.19 V to attain a current density of 10 mA cm<sup>-2</sup> with hydrazine oxidation-assisted water electrolysis. This study not only highlights a new route for low-cost and high-efficiency hydrogen generation

but also demonstrates a highly promising electrode material integrating 3D low-tortuosity porous structure with lattice engineering.

#### CRediT authorship contribution statement

**Zhikai Shi:** Conceptualization, Methodology, Formal analysis, Investigation, Data curation, Writing – original draft, Writing – review & editing. **Chengwei Mao:** Software, Validation, Methodology, Formal analysis. **Lei Zhong:** Data curation, Formal analysis. **Wenhao Pan:** Formal analysis, Investigation. **Jiayao Peng:** Formal analysis, Investigation. **Jianlin Huang:** Project administration, Funding acquisition, Resources, Conceptualization, Writing – review & editing.

#### Declaration of Competing Interest

The authors declare that they have no known competing financial interests or personal relationships that could have appeared to influence the work reported in this paper.

#### Data Availability

Data will be made available on request.

#### Acknowledgements

We gratefully acknowledge the financial support from the National Natural Science Foundation of China (22076049), Guangdong Science and Technology Program (2020B121201003), and Guangzhou Science and Technology Program (B3221440).

#### Appendix A. Supporting information

Supplementary data associated with this article can be found in the online version at [doi:10.1016/j.apcatb.2023.123123](https://doi.org/10.1016/j.apcatb.2023.123123).

## References

- [1] C. Rong, X. Shen, Y. Wang, L. Thomsen, T. Zhao, Y. Li, X. Lu, R. Amal, C. Zhao, Electronic structure engineering of single-atom Ru sites via Co-N4 sites for bifunctional ph-universal water splitting, *Adv. Mater.* 34 (2022), 2110103, <https://doi.org/10.1002/adma.202110103>.
- [2] L. Sun, Q. Luo, Z. Dai, F. Ma, Material libraries for electrocatalytic overall water splitting, *Coord. Chem. Rev.* 444 (2021), 214049, <https://doi.org/10.1016/j.ccr.2021.214049>.
- [3] Z.P. Ifkovits, J.M. Evans, M.C. Meier, K.M. Papadantonakis, N.S. Lewis, Decoupled electrochemical water-splitting systems: a review and perspective, *Energy Environ. Sci.* 14 (2021) 4740–4759, <https://doi.org/10.1039/D1EE01226F>.
- [4] J. Wang, F. Xu, H. Jin, Y. Chen, Y. Wang, Non-noble metal-based carbon composites in hydrogen evolution reaction: fundamentals to applications, *Adv. Mater.* 29 (2017), 1605838, <https://doi.org/10.1002/adma.201605838>.
- [5] A. Zagalskaya, V. Alexandrov, Role of defects in the interplay between adsorbate evolving and lattice oxygen mechanisms of the oxygen evolution reaction in RuO<sub>2</sub> and IrO<sub>2</sub>, *ACS Catal.* 10 (2020) 3650–3657, <https://doi.org/10.1021/acscatal.9b05544>.
- [6] Y. Guo, T. Park, J.W. Yi, J. Henzie, J. Kim, Z. Wang, B. Jiang, Y. Bando, Y. Sugahara, J. Tang, Y. Yamauchi, Nanoarchitectonics for transition-metal-sulfide-based electrocatalysts for water splitting, *Adv. Mater.* 31 (2019), 1807134, <https://doi.org/10.1002/adma.201807134>.
- [7] Z. Shi, Z. Yu, J. Guo, R. Jiang, Y. Hou, Y. Chen, H. Chen, M. Wang, H. Pang, W. Tang, Lattice distortion of crystalline-amorphous nickel molybdenum sulfide nanosheets for high-efficiency overall water splitting: libraries of lone pairs of electrons and in situ surface reconstitution, *Nanoscale* 14 (2022) 1370–1379, <https://doi.org/10.1039/D1NR07438E>.
- [8] H. Tsai, R. Asadpour, J.-C. Blancon, C.C. Stoumpos, O. Durand, J.W. Strzalka, B. Chen, R. Verduzco, P.M. Ajayan, S. Tretiak, J. Even, M.A. Alam, M.G. Kanatzidis, W. Nie, A.D. Mohite, Light-induced lattice expansion leads to high-efficiency perovskite solar cells, *Science* 360 (2018) 67–70, <https://doi.org/10.1126/science.aap8671>.
- [9] Y. Qin, T. Yu, S. Deng, X.-Y. Zhou, D. Lin, Q. Zhang, Z. Jin, D. Zhang, Y.-B. He, H.-J. Qiu, L. He, F. Kang, K. Li, T.-Y. Zhang, RuO<sub>2</sub> electronic structure and lattice strain dual engineering for enhanced acidic oxygen evolution reaction performance, *Nat. Commun.* 13 (2022) 3784, <https://doi.org/10.1038/s41467-022-31468-0>.
- [10] Y. Wang, Y. Jiao, H. Yan, G. Yang, C. Tian, A. Wu, Y. Liu, H. Fu, Vanadium-Incorporated CoP<sub>2</sub> with lattice expansion for highly efficient acidic overall water splitting, *Angew. Chem. Int. Ed.* 61 (2022), e202116233, <https://doi.org/10.1002/anie.202116233>.
- [11] H. Sun, W. Zhang, J.-G. Li, Z. Li, X. Ao, K.-H. Xue, K.K. Ostrikov, J. Tang, C. Wang, Rh-engineered ultrathin NiFe-LDH nanosheets enable highly-efficient overall water splitting and urea electrolysis, *Appl. Catal. B-Environ.* 284 (2021), 119740, <https://doi.org/10.1016/j.apcatb.2020.119740>.
- [12] C. Deng, C.Y. Toe, X. Li, J. Tan, H. Yang, Q. Hu, C. He, Earth-abundant metal-based electrocatalysts promoted anodic reaction in hybrid water electrolysis for efficient hydrogen production: recent progress and perspectives, *Adv. Energy Mater.* 12 (2022), 2201047, <https://doi.org/10.1002/aenm.202201047>.
- [13] D. Wang, J. Li, Y. Zhao, H. Xu, J. Zhao, Bifunctional Cu<sub>2</sub>S–Co(OH)<sub>2</sub> nanotube array/Cu foam electrocatalyst for overall water splitting, *Electrochim. Acta* 316 (2019) 8–18, <https://doi.org/10.1016/j.electacta.2019.05.118>.
- [14] S.J. Patil, N.R. Chodankar, S.-K. Hwang, P.A. Shinde, G. Seeta Rama Raju, K. Shanmugam Ranjith, Y.S. Huh, Y.-K. Han, Co-metal–organic framework derived CoSe<sub>2</sub>@MoSe<sub>2</sub> core–shell structure on carbon cloth as an efficient bifunctional catalyst for overall water splitting, *Chem. Eng. J.* 429 (2022), 132379, <https://doi.org/10.1016/j.cej.2021.132379>.
- [15] H. Zhang, J. Li, S. Xi, Y. Du, X. Hai, J. Wang, H. Xu, G. Wu, J. Zhang, J. Lu, J. Wang, A graphene-supported single-Atom FeN<sub>5</sub> catalytic site for efficient electrochemical CO<sub>2</sub> Reduction, *Angew. Chem. Int. Ed.* 58 (2019) 14871–14876, <https://doi.org/10.1002/anie.201906079>.
- [16] T. Liu, J. Mou, Z. Wu, C. Lv, J. Huang, M. Liu, A facile and scalable strategy for fabrication of superior bifunctional freestanding air electrodes for flexible zinc–air batteries, *Adv. Funct. Mater.* 30 (2020), 2003407, <https://doi.org/10.1002/adfm.202003407>.
- [17] J. Song, C. Chen, S. Zhu, M. Zhu, J. Dai, U. Ray, Y. Li, Y. Kuang, Y. Li, N. Quispe, Y. Yao, A. Gong, U.H. Leiste, H.A. Bruck, J.Y. Zhu, A. Vellore, H. Li, M.L. Minus, Z. Jia, A. Martini, T. Li, L. Hu, Processing bulk natural wood into a high-performance structural material, *Nature* 554 (2018) 224–228, <https://doi.org/10.1038/nature25476>.
- [18] C. Chen, Y. Kuang, S. Zhu, I. Burgert, T. Keplinger, A. Gong, T. Li, L. Berglund, S. J. Eichhorn, L. Hu, Structure–property–function relationships of natural and engineered wood, *Nat. Rev. Mater.* 5 (2020) 642–666, <https://doi.org/10.1038/s41578-020-0195-z>.
- [19] S. Wei, C. Wan, Y. Wu, Recent advances in wood-based electrode materials for supercapacitors, *Green. Chem.* (2023), <https://doi.org/10.1039/D2GC04271A>.
- [20] A. Kumar, T. Jyske, M. Petric, Delignified wood from understanding the hierarchically aligned cellulosic structures to creating novel functional materials: a review, *Adv. Sustain. Syst.* 5 (2021), 2000251, <https://doi.org/10.1002/adusu.202000251>.
- [21] H. Zhu, W. Luo, P.N. Ciesielski, Z. Fang, J.Y. Zhu, G. Henriksson, M.E. Himmel, L. Hu, Wood-derived materials for green electronics, biological devices, and energy applications, *Chem. Rev.* 116 (2016) 9305–9374, <https://doi.org/10.1021/acs.chemrev.6b00225>.
- [22] J. Huang, B. Zhao, T. Liu, J. Mou, Z. Jiang, J. Liu, H. Li, M. Liu, Wood-derived materials for advanced electrochemical energy storage devices, *Adv. Funct. Mater.* 29 (2019), 1902255, <https://doi.org/10.1002/adfm.201902255>.
- [23] W. Gan, L. Wu, Y. Wang, H. Gao, L. Gao, S. Xiao, J. Liu, Y. Xie, T. Li, J. Li, Carbonized wood decorated with cobalt-nickel binary nanoparticles as a low-cost and efficient electrode for water splitting, *Adv. Funct. Mater.* 31 (2021), 2010951, <https://doi.org/10.1002/adfm.202010951>.
- [24] L. Rosenberger, R. Baird, E. McCullen, G. Auner, G. Shreve, XPS analysis of aluminum nitride films deposited by plasma source molecular beam epitaxy, *Surf. Interface Anal.* 40 (2008) 1254–1261, <https://doi.org/10.1002/sia.2874>.
- [25] Y. Wang, J. Zhao, W. Hou, Y. Xu, Decoration of CdS nanowires with Ni<sub>3</sub>S<sub>4</sub> nanoballs enhancing H<sub>2</sub> and H<sub>2</sub>O<sub>2</sub> production under visible light, *Appl. Catal. B-Environ.* 310 (2022), 121350, <https://doi.org/10.1016/j.apcatb.2022.121350>.
- [26] K. Wan, J. Luo, C. Zhou, T. Zhang, J. Arbiol, X. Lu, B.-W. Mao, X. Zhang, J. Fransser, Hierarchical porous Ni<sub>3</sub>S<sub>4</sub> with enriched high-valence Ni sites as a robust electrocatalyst for efficient oxygen evolution reaction, *Adv. Funct. Mater.* 29 (2019), 1900315, <https://doi.org/10.1002/adfm.201900315>.
- [27] J. Mou, Y. Li, L. Ou, J. Huang, A highly-efficient electrocatalyst for room temperature sodium-sulfur batteries: assembled nitrogen-doped hollow porous carbon spheres decorated with ultrafine α-MoCl<sub>3</sub> nanoparticles, *Energy Storage Mater.* 52 (2022) 111–119, <https://doi.org/10.1016/j.ensm.2022.07.028>.
- [28] F. Chen, A.S. Gong, M. Zhu, G. Chen, S.D. Lacey, F. Jiang, Y. Li, Y. Wang, J. Dai, Y. Yao, J. Song, B. Liu, K. Fu, S. Das, L. Hu, Mesoporous, three-dimensional wood membrane decorated with nanoparticles for highly efficient water treatment, *ACS Nano* 11 (2017) 4275–4282, <https://doi.org/10.1021/acsnano.7b01350>.
- [29] H. Li, Q. Zhang, C.C.R. Yap, B.K. Tay, T.H.T. Edwin, A. Olivier, D. Baillargeat, From bulk to monolayer MoS<sub>2</sub>: evolution of raman scattering, *Adv. Funct. Mater.* 22 (2012) 1385–1390, <https://doi.org/10.1002/adfm.201102111>.
- [30] M. Gao, L. Wang, Y. Yang, Y. Sun, X. Zhao, Y. Wan, Metal and metal oxide supported on ordered mesoporous carbon as heterogeneous catalysts, *ACS Catal.* 13 (2023) 4060–4090, <https://doi.org/10.1021/acscatal.2c05894>.
- [31] B. Zhou, Y. Li, Y. Zou, W. Chen, W. Zhou, M. Song, Y. Wu, Y. Lu, J. Liu, Y. Wang, S. Wang, Platinum modulates redox properties and 5-hydroxymethylfurfural adsorption kinetics of Ni(OH)<sub>2</sub> for biomass upgrading, *Angew. Chem. Int. Ed.* 60 (2021) 22908–22914, <https://doi.org/10.1002/anie.202109211>.
- [32] J. Balamurugan, T.T. Nguyen, D.H. Kim, N.H. Kim, J.H. Lee, 3D nickel molybdenum oxyselenide (Ni<sub>1-x</sub>MoxOSe) nanoarchitectures as advanced multifunctional catalyst for Zn-air batteries and water splitting, *Appl. Catal. B-Environ.* 286 (2021), 119909, <https://doi.org/10.1016/j.apcatb.2021.119909>.
- [33] W. Zhang, M. Li, L. Zhong, J. Huang, M. Liu, A family of MOFs@Wood-Derived hierarchical porous composites as freestanding thick electrodes of solid supercapacitors with enhanced areal capacitances and energy densities, *Mater. Today Energy* 24 (2022), 100951, <https://doi.org/10.1016/j.mtener.2022.100951>.
- [34] D. Wu, X. Xie, J. Zhang, Y. Ma, C. Hou, X. Sun, X. Yang, Y. Zhang, H. Kimura, W. Du, Embedding NiS nanoflakes in electrospun carbon fibers containing NiS nanoparticles for hybrid supercapacitors, *Chem. Eng. J.* 446 (2022), 137262, <https://doi.org/10.1016/j.cej.2022.137262>.
- [35] Y. Zhao, H. Wu, Y. Wang, L. Liu, W. Qin, S. Liu, J. Liu, Y. Qin, D. Zhang, A. Chu, B. Jia, X. Qu, M. Qin, Sulfur coordination engineering of molybdenum single-atom for dual-functional oxygen reduction/evolution catalysis, *Energy Storage Mater.* 50 (2022) 186–195, <https://doi.org/10.1016/j.ensm.2022.05.015>.
- [36] Z. Wang, Q. Lei, Z. Wang, H. Yuan, L. Cao, N. Qin, Z. Lu, J. Xiao, J. Liu, In-situ synthesis of free-standing FeNi<sub>2</sub>-oxyhydroxide nanosheets as a highly efficient electrocatalyst for water oxidation, *Chem. Eng. J.* 395 (2020), 125180, <https://doi.org/10.1016/j.cej.2020.125180>.
- [37] M. Ayiania, M. Smith, A.J.R. Hensley, L. Scudiero, J.-S. McEwen, M. Garcia-Perez, Deconvoluting the XPS spectra for nitrogen-doped chars: an analysis from first principles, *Carbon* 162 (2020) 528–544, <https://doi.org/10.1016/j.carbon.2020.02.065>.
- [38] S.Y. Tee, D. Ponsford, C.L. Lay, X. Wang, X. Wang, D.C.J. Neo, T. Wu, W. Thitsartarn, J.C.C. Yeo, G. Guan, T.-C. Lee, M.-Y. Han, Thermoelectric silver-based chalcogenides, *Adv. Sci.* 9 (2022), 2204624, <https://doi.org/10.1002/advs.202204624>.
- [39] H. Chen, T. Liu, J. Mou, W. Zhang, Z. Jiang, J. Liu, J. Huang, M. Liu, Free-standing N-self-doped carbon nanofiber aerogels for high-performance all-solid-state supercapacitors, *Nano Energy* 63 (2019), 103836, <https://doi.org/10.1016/j.nanoen.2019.06.032>.
- [40] J. Hao, Z. Zhuang, K. Cao, G. Gao, C. Wang, F. Lai, S. Lu, P. Ma, W. Dong, T. Liu, M. Du, H. Zhu, Unraveling the electronegativity-dominated intermediate adsorption on high-entropy alloy electrocatalysts, *Nat. Commun.* 13 (2022) 2662, <https://doi.org/10.1038/s41467-022-30379-4>.
- [41] D. Liu, Y. Yan, H. Li, D. Liu, Y. Yang, T. Li, Y. Du, S. Yan, T. Yu, W. Zhou, P. Cui, Z. Zou, A. Template Editing, Strategy to create interlayer-confined active species for efficient and durable oxygen evolution reaction, *Adv. Mater.* 35 (2023), 2203420, <https://doi.org/10.1002/adma.202203420>.
- [42] J. Huang, Y. Li, Y. Zhang, G. Rao, C. Wu, Y. Hu, X. Wang, R. Lu, Y. Li, J. Xiong, Identification of key reversible intermediates in self-reconstructed nickel-based hybrid electrocatalysts for oxygen evolution, *Angew. Chem. Int. Ed.* 58 (2019) 17458–17464, <https://doi.org/10.1002/anie.201910716>.
- [43] O. Diaz-Morales, D. Ferrus-Suspedra, M.T.M. Koper, The importance of nickel oxyhydroxide deprotonation on its activity towards electrochemical water oxidation, *Chem. Sci.* 7 (2016) 2639–2645, <https://doi.org/10.1039/C5SC04486C>.
- [44] J. Zhang, Y. Li, X. Liang, Q. Liu, Q. Chen, M. Chen, Sulfur vacancies engineered Ni<sub>3</sub>S<sub>4</sub>-x hollow microspheres with optimized anionic adsorption energy for high-

- performance supercapacitor, *Small* 18 (2022), 2106074, <https://doi.org/10.1002/smll.202106074>.
- [45] J.H. Choi, S.-K. Park, Y.C. Kang, N-doped carbon coated Ni-Mo sulfide tubular structure decorated with nanobubbles for enhanced sodium storage performance, *Chem. Eng. J.* 383 (2020), 123112, <https://doi.org/10.1016/j.cej.2019.123112>.
- [46] D. Liu, L. Yang, J. Wu, B. Li, Tuning sulfur vacancies in CoS<sub>2</sub> via a molten salt approach for promoted mercury vapor adsorption, *Chem. Eng. J.* 450 (2022), 137956, <https://doi.org/10.1016/j.cej.2022.137956>.
- [47] Y. Duan, Z.-Y. Yu, S.-J. Hu, X.-S. Zheng, C.-T. Zhang, H.-H. Ding, B.-C. Hu, Q.-Q. Fu, Z.-L. Yu, X. Zheng, J.-F. Zhu, M.-R. Gao, S.-H. Yu, Scaled-up synthesis of amorphous NiFeMo oxides and their rapid surface reconstruction for superior oxygen evolution catalysis, *Angew. Chem. Int. Ed.* 58 (2019) 15772–15777, <https://doi.org/10.1002/anie.201909939>.
- [48] Y. Yu, N. Li, X. Lu, B. Yan, G. Chen, Y. Wang, X. Duan, Z. Cheng, S. Wang, Co/N co-doped carbonized wood sponge with 3D porous framework for efficient peroxymonosulfate activation: Performance and internal mechanism, *J. Hazard. Mater.* 421 (2022), 126735, <https://doi.org/10.1016/j.jhazmat.2021.126735>.
- [49] Y. Zhu, K. Fan, C.-S. Hsu, G. Chen, C. Chen, T. Liu, Z. Lin, S. She, L. Li, H. Zhou, Y. Zhu, H.M. Chen, H. Huang, Supported Ruthenium Single-Atom and Clustered Catalysts Outperform Benchmark Pt for Alkaline Hydrogen Evolution, *Adv. Mater.*, n/a 2301133, <https://doi.org/10.1002/adma.202301133>.
- [50] J. Chen, T. Yu, Z. Zhai, G. Qian, S. Yin, Coupling interface engineering with electronic interaction toward high-efficiency H<sub>2</sub> evolution in pH-universal electrolytes, *J. Energy Chem.* 80 (2023) 535–541, <https://doi.org/10.1016/j.jechem.2023.01.060>.
- [51] B. Tian, H. Shin, S. Liu, M. Fei, Z. Mu, C. Liu, Y. Pan, Y. Sun, W.A. Goddard III, M. Ding, Double-exchange-induced in situ conductivity in nickel-based oxyhydroxides: an effective descriptor for electrocatalytic oxygen evolution, *Angew. Chem. Int. Ed.* 60 (2021) 16448–16456, <https://doi.org/10.1002/anie.202101906>.
- [52] L. Bai, S. Lee, X. Hu, Spectroscopic and electrokinetic evidence for a bifunctional mechanism of the oxygen evolution reaction, *Angew. Chem. Int. Ed.* 60 (2021) 3095–3103, <https://doi.org/10.1002/anie.202011388>.
- [53] M. Yu, E. Budiyo, H. Tüysüz, Principles of water electrolysis and recent progress in cobalt-, nickel-, and iron-based oxides for the oxygen evolution reaction, *Angew. Chem. Int. Ed.* 61 (2022), e202103824, <https://doi.org/10.1002/anie.202103824>.
- [54] Y. Zhao, X.F. Lu, Z.-P. Wu, Z. Pei, D. Luan, X.W. Lou, Supporting Trimetallic Metal-Organic Frameworks on S/N-Doped Carbon Macroporous Fibers for Highly Efficient Electrocatalytic Oxygen Evolution, *Adv. Mater.*, n/a 2207888, <https://doi.org/10.1002/adma.202207888>.